

UNIVERSIDADE FEDERAL DE MINAS GERAIS

Escola de Engenharia

Programa de Pós-Graduação em Engenharia Química

Márcio Ribeiro Vianna Neto

Synthesis and optimization of Kraft process evaporator plants

BELO HORIZONTE – MG

2021

Márcio Ribeiro Vianna Neto

Synthesis and optimization of Kraft process evaporator plants

Dissertation for the degree of Doctor of Science (Technology) to be presented with due permission for public examination and criticism at Lappeenranta-Lahti University of Technology LUT, Lappeenranta, Finland on the 9th of March, 2021, at 4 PM, Finnish time. The dissertation was written under a joint supervision (cotutelle) agreement between Lappeenranta-Lahti University of Technology LUT, Finland and the Federal University of Minas Gerais, Brazil and jointly supervised by supervisors from both universities.

Field of study: Process simulation and optimization

Supervisors: Esa Kari Vakkilainen (LUT) and Éder Domingos Oliveira (UFMG)

BELO HORIZONTE – MG

2021

V617s

Vianna Neto, Márcio Ribeiro.

Synthesis and optimization of Kraft process evaporator plants
[recurso eletrônico] / Márcio Ribeiro Vianna Neto. – 2021.

1 recurso online (95 f. : il., color.) : pdf.

Orientador: Éder Domingos Oliveira.

Orientador: Esa Kari Vakkilainen.

Tese (doutorado) – Universidade Federal de Minas Gerais,
Escola de Engenharia.

Anexos: f. 103-106.

Bibliografia: f. 96-102.

Exigências do sistema: Adobe Acrobat Reader.

1. Engenharia química - Teses. 2. Celulose - Teses. 3. Otimização
- Teses. 4. Papel - Teses. 5. Polpação alcalina por sulfato - Teses.

I. Oliveira, Éder Domingos. II. Vakkilainen, Esa K. III. Universidade
Federal de Minas Gerais. Escola de Engenharia. IV. Título.

CDU: 66.0(043)



UNIVERSIDADE FEDERAL DE MINAS GERAIS
ESCOLA DE ENGENHARIA
PROGRAMA DE PÓS-GRADUAÇÃO EM ENGENHARIA QUÍMICA

FOLHA DE APROVAÇÃO

"SYNTHESIS AND OPTIMIZATION OF KRAFT PROCESS EVAPORATOR PLANTS"

Márcio Ribeiro Vianna Neto

Tese submetida à Banca Examinadora designada pelo Colegiado do Programa de Pós-Graduação em Engenharia Química da Escola de Engenharia da Universidade Federal de Minas Gerais, como parte dos requisitos à obtenção do título de DOUTOR EM ENGENHARIA QUÍMICA.

54ª TESE APROVADA EM 9 DE MARÇO DE 2021 POR:



Documento assinado eletronicamente por Eder Domingos de Oliveira, Professor do Magistério Superior, em 09/03/2021, às 14:14, conforme horário oficial de Brasília, com fundamento no art. 5º do [Decreto nº 10.543, de 13 de novembro de 2020](#).



Documento assinado eletronicamente por Daniel Moreira Saturnino, Usuário Externo, em 09/03/2021, às 14:16, conforme horário oficial de Brasília, com fundamento no art. 5º do [Decreto nº 10.543, de 13 de novembro de 2020](#).



Documento assinado eletronicamente por Nikolai Angelo de Martini, Usuário Externo, em 09/03/2021, às 14:17, conforme horário oficial de Brasília, com fundamento no art. 5º do [Decreto nº 10.543, de 13 de novembro de 2020](#).



Documento assinado eletronicamente por Vakkilainen, Esa Kari, Usuário Externo, em 09/03/2021, às 14:45, conforme horário oficial de Brasília, com fundamento no art. 5º do [Decreto nº 10.543, de 13 de novembro de 2020](#).



Documento assinado eletronicamente por Rodney Rezende Saldanha, Membro de comissão, em 09/03/2021, às 15:05, conforme horário oficial de Brasília, com fundamento no art. 5º do [Decreto nº 10.543, de 13 de novembro de 2020](#).



Documento assinado eletronicamente por Song Won Park, Usuário Externo, em 09/03/2021, às 16:05, conforme horário oficial de Brasília, com fundamento no art. 5º do [Decreto nº 10.543, de 13 de novembro de 2020](#).



A autenticidade deste documento pode ser conferida no site https://sei.ufmg.br/sei/controlador_externo.php?acao=documento_conferir&id_orgao_acesso_externo=0, informando o código verificador 0598875 e o código CRC 39A85E86.

*To my parents Marcos Rocha Vianna and Rita Maria Pinto
Coelho Vianna, to whom I owe all that is best in me.*

Acknowledgements

I would personally like to thank my supervisor, Prof. Esa K. Vakkilainen from the School of Energy Systems at Lappeenranta-Lahti University of Technology (LUT), for his patience, willingness to help, and invaluable advice, without which this dissertation would not have been possible. I would also like to thank my supervisor, Prof. Éder D. Oliveira from the Department of Chemical Engineering at Universidade Federal de Minas Gerais (UFMG), for his guidance and solicitude, even in the most adverse circumstances.

My special thanks to Prof. Marcelo Cardoso from the Department of Chemical Engineering at UFMG for his continuous support, expert advice, and friendship throughout the years.

My special thanks also to Dr. Jussi Saari, with whom I have worked since 2013, and it has always been a thought-provoking and thoroughly enjoyable experience.

This work was carried out in the Department of Energy and Environmental Technology at Lappeenranta-Lahti University of Technology (LUT), Finland, between 2017 and 2018 and in the Department of Chemical Engineering at Universidade Federal de Minas Gerais, Brazil, between 2017 and 2020. It took the help of many people from both institutions to finalize this dissertation, but I would like to send my special thanks to Sari Damsten-Puustinen for her solicitude and willingness to help me with the internal procedures at LUT, even from a distance. It is fair to say that, without her help, this dissertation would not have come to fruition. Likewise, my thanks to Fernanda Moura de Abreu for all her help through the years with the internal procedures at UFMG.

Many other people contributed indirectly to this work. The list would be far too large to write, but I would like to send my special thanks to Débora Goulart Faria for her continuous feedback and support. My special thanks also go to Ekaterina Sermyagina, Manuel García Pérez, and Juha Kaikko for their feedback, ideas, and very pleasant and much needed coffee breaks.

My special thanks to my always supportive parents, Marcos Rocha Vianna and Rita Maria Pinto Coelho Vianna, who have provided me with all that I needed for this work.

My special thanks also go for Bernardo Teixeira, for his seemingly endless friendship and support.

I am also indebted to the Conselho Nacional de Desenvolvimento Científico e Tecnológico (CNPq/BRAZIL), Fundação de Amparo à Pesquisa do Estado de Minas Gerais (Fapemig/BRAZIL), and Academy of Finland for supporting this study.

Márcio R. V. Neto
November 2020
Nova Lima, Brazil

Resumo

Márcio R. V. Neto

Síntese e otimização de plantas de evaporação no processo Kraft

Nesta tese é descrita uma nova metodologia para síntese e otimização de sistemas de evaporadores de múltiplo efeito baseada em superestruturas de processo. A metodologia permite que sistemas de evaporadores de múltiplo efeito sejam otimizados levando em conta, simultaneamente, a sua estrutura e as áreas de troca térmica, sem haver a necessidade de recorrer a estruturas predeterminadas. A metodologia foi aplicada a estudos de caso em que era necessário especificar e posicionar novos corpos evaporadores em sistemas pré-existentes cuja capacidade deveria ser aumentada. Um simulador orientado a equações para plantas de evaporação foi desenvolvido e utilizado em conjunto com o algoritmo de otimização estocástica Evolução Diferencial. Um sequencial modular foi também desenvolvido para comparação. Plantas de evaporação de múltiplo efeito foram tomadas como estudos de caso para destacar o funcionamento do novo método e para avaliar sua viabilidade de aplicação em sistemas realistas. Através desta metodologia, foi possível determinar o arranjo ótimo e as áreas de transferência de calor correspondentes aos sistemas estudados.

Palavras-chave: síntese de processos, otimização de processos, processo Kraft, evaporação de múltiplo efeito, papel e celulose

Abstract

Márcio R. V. Neto

Synthesis and optimization of kraft process evaporator plants

In this dissertation, a novel methodology based on process superstructures for the synthesis and optimization of multiple-effect evaporation systems is described. The methodology allows for the structure and heat transfer areas of multiple-effect evaporation systems to be simultaneously considered in optimization without having to resort to any previously selected arrangements. The methodology is applied to industrial evaporator case studies where it is necessary to simultaneously size and determine the best way to arrange additional evaporator bodies in an existing system to increase maximum load. An equation-oriented simulator for chemical pulp mill evaporator plants was developed and used in conjunction with differential evolution. A sequential-modular simulator was also developed for comparison. Multiple-effect evaporator plants were used as case studies to highlight the workings of the new method and to assess its viability in realistic systems. Through this methodology, it was possible to determine the optimal arrangement and heat transfer areas for the studied systems.

Keywords: process synthesis, process optimization, Kraft process, multiple-effect evaporation, pulp and paper

List of publications

In the process of this dissertation, the following papers were published. The rights have been granted by the publishers to include the papers in the dissertation.

- I. Vianna Neto, M. R., Saari, J., Vakkilainen, E. K., Cardoso, M., and Oliveira, E. D. (2020) A superstructure-based methodology for simultaneously sizing and arranging additional evaporator bodies in multiple-effect evaporator plants. *Journal of Science and Technology for Forest Products and Processes*, Vol. 7, pp. 36–47.
- II. Vianna Neto, M. R., Cardoso, M., Vakkilainen, E. K., and Oliveira, E. D. (2020a) Development of a steady-state kraft evaporation plant simulator for process optimization. *O Papel*, Vol. 81, pp. 83–89.
- III. Vianna Neto, M. R., Cardoso, M., Vakkilainen, E. K., and Oliveira, E. D. (2020b) Improving an equation-oriented steady-state evaporation plant simulator with a more robust evaporator model. Proceedings of the International Chemical Recovery Conference 2020
- IV. Vianna Neto, M. R., Cardoso, M., Sermyagina, E., Vakkilainen, E. K., and Oliveira, E. D. (2020) Designing a sequential-modular steady-state simulator for kraft recovery cycle evaporative systems. Proceedings of the 53rd Pulp and Paper International Congress and Exhibition.

Author's contribution

- I. The author was the principal author and investigator for all the above papers. The author created the evaporator simulation model, collected the data, was responsible for its analysis, and wrote the manuscript. Dr. Saari helped in implementing the optimization algorithm and debugging it. Professors Vakkilainen, Cardoso, and Oliveira supervised the work and gave valuable comments and suggestions during the course of the research.
- II. The author was the principal author and investigator in Paper II. Professors Cardoso, Vakkilainen, and Oliveira supervised the work and gave valuable comments and suggestions during the course of the research.

- III. The author was the principal author and investigator in Paper III. Professors Cardoso, Vakkilainen, and Oliveira supervised the work and gave valuable comments and suggestions during the course of the research.
- IV. The author was the principal author and investigator in Paper IV. Professors Cardoso, Vakkilainen, and Oliveira supervised the work and gave valuable comments and suggestions during the course of the research.

Other publications not included in this dissertation

The author of this dissertation has contributed to studies on the optimization of heat exchangers in the related publications not included in the dissertation:

- V. Saari Jussi, Garcia Perez Manuel, Vianna Neto Marcio, Cardoso Marcelo, Vakkilainen Esa, and Kaikko Juha. (2019) Shell-and-tube heat exchanger optimization - considering problem formulation and tuning for different types of methods. Proceedings HEFAT 2019 14th International Conference on Heat Transfer, Fluid Mechanics and Thermodynamics.
- VI. Saari Jussi, Garcia Perez Manuel, Vianna Neto Marcio, Cardoso Marcelo, Vakkilainen Esa, and Kaikko Juha. (2019) Shell-and-tube heat exchanger optimization - impact of problem formulation and cost function. Proceedings HEFAT 2019 14th International Conference on Heat Transfer, Fluid Mechanics and Thermodynamics.
- VII. Saari Jussi, Neto Márcio, Cardoso Marcelo, Mankonen Alekski, Kaikko Juha, and Vakkilainen Esa. (2020) Techno-economic optimization of a back pressure condenser in a small cogeneration plant with a novel greedy cuckoo search algorithm. Proceedings of the International Conference on Efficiency, Cost, Optimization, Simulation and Environmental Impact of Energy Systems. 33rd International Conference on Efficiency, Cost, Optimization, Simulation and Environmental Impact of Energy Systems (ECOS 2020).

Nomenclature

Latin alphabet

A	area	m^2
b_j^L	lower bound for j^{th} variable	
b_j^U	upper bound for j^{th} variable	
\mathbf{B}	BFGS approximate Hessian matrix	
BPR	boiling point rise	$^{\circ}C$
c	cost	US\$
CR	crossover probability	
c_p	heat capacity	$kJ/kg.K$
D	number of choice variables	
f_{obj}	objective function	
F	scale factor	
h	convective heat transfer coefficient	$kW/m^2.K$
H	enthalpy	kJ/kg
$H_{w,80}$	water enthalpy at $80^{\circ}C$	kJ/kg
\mathbf{H}	Hessian matrix	
k	thermal conductivity	$kW/m.K$
L	characteristic length	m
\mathbf{L}	loop matrix	
\dot{m}	mass flow	kg/s
M	maximum bipartite matching	
n_{neg}	number of negative variables	
N_p	population size	
N_{trials}	number of trials	
P	absolute pressure	Pa
\mathbf{p}	BFGS step direction	
\mathbf{q}	BFGS gradient difference vector	
\dot{Q}	heat flow	kW
r	uniformly sampled number between 0 and 1	
t	temperature	$^{\circ}C$
T	absolute temperature	K
T_P	water boiling temperature at pressure P	K
U	global heat transfer coefficient	$kW/m^2.K$
v	velocity	m/s
\mathbf{u}	trial vector	
\mathbf{v}	target vector	
x_D	dissolved solids fraction	
x_T	total solids fraction	

Greek alphabet

α_n	Step-control parameter
------------	------------------------

μ	Dynamic viscosity	Pa.s
ρ	Specific mass	kg/m ³

Dimensionless numbers

Nu	Nusselt number
Pr	Prandtl number
Re	Reynolds number

Superscripts

bp	boiling point
----	---------------

Subscripts

atm	atmospheric
bp	boiling point
lam	laminar
liq	liquid
neg	negative
par	parallel
sat	saturation
ser	series
surf	surface
turb	turbulent
vap	vapor
w	water

Abbreviations

API	application-programmer interface
BFGS	Broyden-Fletcher-Goldfarb-Shanno
BPR	boiling point rise
CHP	combined heat and power
DE	differential evolution
DFS	depth-first search
EOA	equation-oriented approach
FF	falling film
GSOE	global system of equations
GUI	graphical user interface
IAPWS	International Association for the Properties of Water and Steam
LTV	long-tube vertical
LP	linear programming
MEE	multiple-effect evaporation
MILP	mixed-integer linear programming
NFE	number of function evaluations
NR	Newton-Raphson

SCC strongly connected component
SMA sequential-modular approach

Contents

Acknowledgements

Abstract

Contents

List of publications **10**

Nomenclature **13**

1 Introduction **19**

- 1.1 Aim and scope 20
- 1.2 Additional information 20

2 Literature review **23**

- 2.1 Chemical recovery in the pulp and paper industry 23
 - 2.1.1 Chemical recovery cycle 23
 - 2.1.2 Black liquor evaporation 25
 - 2.1.3 Condensate flashing 27
 - 2.1.4 Evaporator types 28
 - 2.1.4.1 Falling film evaporators 28
 - 2.1.4.2 Rising film evaporators 29
 - 2.1.4.3 Concentrators 30
 - 2.1.5 Mass and energy balances in evaporators 30
- 2.2 Simulation and optimization of evaporative systems 33
 - 2.2.1 Linear and mixed integer linear programming 33
 - 2.2.2 Nonlinear programming 35
- 2.3 General process simulation techniques 37
 - 2.3.1 Sequential-modular approach 39
 - 2.3.2 Equation-oriented approach 41
- 2.4 Mathematical optimization 42
 - 2.4.1 General aspects 42
 - 2.4.2 Deterministic algorithms 43
 - 2.4.3 Stochastic algorithms and differential evolution 46

3 Methodology **51**

- 3.1 EOA simulator architecture 52
- 3.2 SMA simulator architecture 55
- 3.3 Supported unit processes, blocks, and streams 57
 - 3.3.1 A simplified evaporator model 59
- 3.4 Physical properties 60
- 3.5 Base scenarios 61

3.6	Model validation.....	62
3.7	Expanding the base scenarios using the EOA simulator.....	63
3.7.1	Calculations.....	66
3.7.2	Optimization parameters.....	67
3.8	Improving the convergence characteristics of the EOA simulator.....	70
3.8.1	Test cases.....	72
3.8.2	Convergence rate assessment.....	73
3.9	Convergence characteristics of the SMA simulator.....	74
3.9.1	Test scenarios.....	75
4	Results and discussion	79
4.1	Simplified model.....	79
4.2	Evaporator model validation.....	81
4.3	Expanding the base scenarios using the EOA simulator.....	83
4.4	Improving the convergence characteristics of the EOA simulator.....	86
4.5	Convergence characteristics of the SMA simulator.....	90
4.6	Discussion.....	92
4.6.1	Theoretical implications.....	92
4.6.2	Practical implications.....	93
5	Conclusions	95
	References	97
	Publications	

1 Introduction

Chemical recovery plants are a fundamentally important subprocess in chemical pulping plants and are known to be highly energy intensive. Increasing their energy efficiency would not only give their operators a competitive edge, but would also allow more energy to be available for power generation, thus lowering carbon dioxide emissions from fossil fuels, which is key for sustainable development.

When wood is chemically pulped to cellulose, a residue composed of organic and inorganic chemicals is generated. This residue is called black liquor, and it is burned in the recovery boiler, which generates power and recovers part of the chemicals necessary to pulp wood. To ensure that the liquor is effectively burned, its water content needs to be reduced to a dry solids mass fraction of about 80–85%. This is carried out in a multiple-effect evaporator train, usually composed of 5–7+ evaporator bodies. Due to the relatively high latent heat needed to vaporize water, this process requires a considerable amount of energy. In fact, evaporation accounts for 24–30% of the total energy used in a pulp mill.

The optimization of evaporation systems is, therefore, an important goal, for which reason there has been a significant effort in recent studies to address the modeling and optimization of evaporator systems. This is not a trivial task due to the complexity of the mathematical description of such systems. Commonly, given an evaporator plant of interest or a set of predetermined arrangements, a model composed of a system of mostly nonlinear equations that describe it is constructed. The model is then utilized, along with optimization algorithms, to minimize or maximize some variable of interest, such as the total heat transfer area or some measure of cost.

However, the methodologies described so far assume that the arrangement of evaporators, vapor streams, and black liquor streams is known a priori. In practice, this may not be the case. In a situation where an existing evaporator system needs to, for instance, be expanded, the arrangement may not be immediately clear:

- a) How many evaporator bodies should be added, and what is their required heat transfer area?
- b) Should they be added in series with a pre-existent system, in parallel, or a combination thereof?
- c) How would the addition of a new evaporator body affect the energetic efficiency of the chemical recovery cycle?

Likewise, during the design stage of a new evaporator plant, its final arrangement may be unknown. The designers, therefore, would need to decide on the number of effects and what arrangement should be selected. These questions are not trivial due to the potentially large set of different possible arrangements that must be considered, which is especially true for larger systems. The problem becomes even more complex if, as is often the case,

different combinations of variables, such as the heat transfer area or black liquor inflow rate, need to be considered for each arrangement.

It is thus desirable to have a methodology that allows evaporator systems to simultaneously be optimized both with respect their arrangement and any other variables of interest, without having to resort to any predetermined configurations.

1.1 Aim and scope

This work, thus, develops a methodology that allows for evaporator systems to simultaneously be optimized both with respect to their arrangement and any other variables of interest, without having to resort to any predetermined configurations. The methodology is based on developing a robust steady-state simulation engine and pairing it with the well-known differential evolution stochastic optimization algorithm.

This research is predicated on the hypothesis that it is possible to construct a steady-state process simulator for evaporator systems that is robust enough to converge reliably for a potentially large set of possible evaporator arrangements. Moreover, it is also hypothesized that the proposed methodology will converge in a reasonable computational time. To put it succinctly, the research hypothesis is as follows:

Research hypothesis: It is possible to simultaneously optimize evaporator systems both with respect to their topological arrangement and other internal design variables using mathematical optimization techniques.

The following questions are tackled in the research project:

- a) What mathematical difficulties arise when modeling an evaporator system?
- b) What numerical methods are best suited to solving the model?
- c) Is differential evolution well suited to performing this type of optimization? If so, are there any optimal ranges for its parameters?
- d) How well does the proposed methodology scale as the problems grow more complex?

The proposed methodology is novel, as it presents a unified methodology for optimizing the structural arrangement and any other variables of evaporator systems, which would help engineers optimize their existent systems. It may also aid professionals in designing optimal evaporator systems without having to resort to trial and error. The methodology has, therefore, the potential to be applied in the pulp and paper industry.

1.2 Additional information

This research was made possible due to a collaboration between the Department of Chemical Engineering at Universidade Federal de Minas Gerais (UFMG) and the Department of Energy Systems at Lappeenranta-Lahti University of Technology (LUT), which allowed the author to pursue a double doctoral degree.

2 Literature review

2.1 Chemical recovery in the pulp and paper industry

In the pulp and paper industry, cellulosic fibers are disassociated from the lignin found in wood, bagasse, straw, and other raw materials to produce what is referred to as pulp (Cardoso, de Oliveira and Passos, 2009). Once the pulp has been extracted, it can then be processed to produce paper, paperboard, and other cellulosic materials. This process, which is called pulping, can be either mechanical or chemical.

The most common pulping method employed to produce wood pulps is the Kraft process (Cardoso, de Oliveira and Passos, 2009). With this method, wood chips are cooked with a solution of sodium sulfide (Na_2S) and sodium hydroxide (NaOH), called white liquor, which causes cellulose to dissociate from the lignin to which it was bound. Once the cooking process is finished, the pulp is washed to remove spent cooking chemicals and any dissolved organic components (Tikka, 2008). The residue obtained from this washing step is a black alkaline liquid known as black liquor, and, until the 1930s, it was common practice to discard it (Tikka, 2008).

As pulping mills grew larger and new equipment was developed, it became economically feasible to process the black liquor in order to regenerate the chemicals spent in the cooking process. This process is known as the chemical recovery cycle, and it is nowadays fundamental for making the Kraft process economically feasible (Tikka, 2008; Cardoso *et al.*, 2009). The core piece of equipment used in recovery cycle is the so-called recovery boiler, which not only regenerates part of the spent chemicals, but also allows for energy to be produced in a pulping plant (Vakkilainen, 2007; Tikka, 2008).

2.1.1 Chemical recovery cycle

Figure 2-1 is a simplified diagram describing the steps of the chemical recovery cycle. After the cooking process, the Na_2S that was present in the white liquor is oxidized to sodium sulfate, Na_2SO_4 . To revert it back to Na_2S , it needs to be reduced, a process that takes place in the recovery boiler. Well-operated recovery boilers can reduce almost all sulfate back to sulfide (Adams and Frederick, 1988; Adams *et al.*, 1997). The recovery boiler is a very complex heterogeneous system where many reactions take place simultaneously under conditions of high temperature and pressure (Vakkilainen, 2007). Due to its central role in the recovery cycle and also its complexity, it is not surprising that so much space in the technical literature is dedicated to its proper modeling and optimization (Almeida *et al.*, 2000; Costa, Biscaia Jr and Lima, 2004; Ferreira, Cardoso and Park, 2010; Saturnino, 2012).

The products of the recovery boiler reactions include Na_2S and Na_2CO_3 , which come out in molten form and have mass fractions of approximately 23% and 74%, respectively

(Adams and Frederick, 1988; Adams *et al.*, 1997). This molten mixture of Na_2S and Na_2CO_3 is the so-called smelt.

The black liquor produced in the washing process has a relatively low dry solids mass fraction and is usually termed weak black liquor. For the liquor to be efficiently burned in the boiler, its dry solids mass fraction needs to be increased. This is done by leading the liquor through an evaporation plant. The more concentrated liquor emerging from the MEE plant that is then sent to the boiler is termed strong black liquor. Strong black liquor is remarkably more dense and viscous than weak black liquor, and, in order to maintain its viscosity under the applicability limits for centrifugal pumps, it must be kept at temperatures on the order of 100°C (Ramamurthy, Van Heiningen and Kubes, 1993; Zaman, Wight and Fricke, 1994; Andreuccetti, Leite and D'Angelo, 2011; Bajpai, 2016).

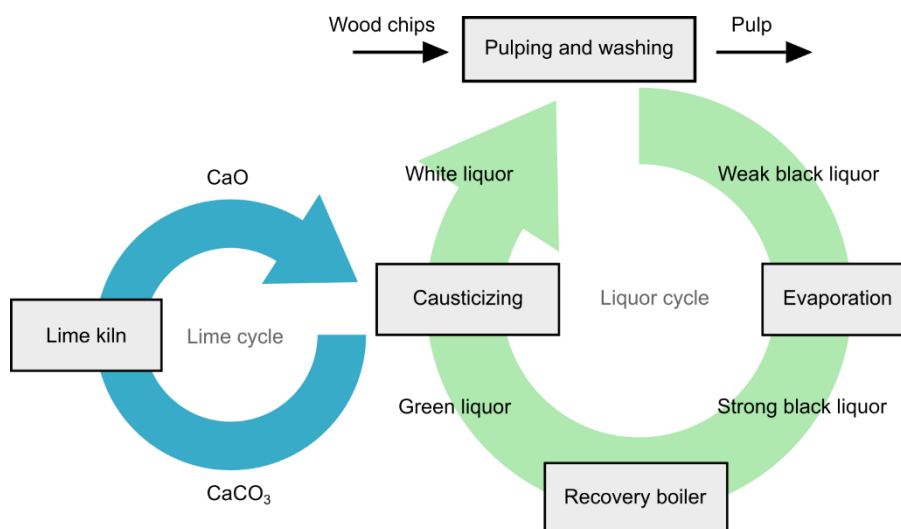


Figure 2-1: Simplified diagram of the chemical recovery cycle.

In the recovery boiler, the water brought in by the liquor is converted to high-pressure steam, which is then fed to turbines, thus generating power. Modern recovery boilers are designed to withstand steam pressures on the order of 9.2 MPa and temperatures on the order of 490°C (Vakkilainen, 2016). The smelt, on the other hand, is dissolved in water, producing the so-called green liquor, a solution containing Na_2S and Na_2CO_3 .

The green liquor is mixed with lime (CaO) in a causticizing plant. The reaction of CaO with Na_2CO_3 regenerates NaOH and generates CaCO_3 , which precipitates out of the solution. Both Na_2S and NaOH have thus been regenerated, and they can be fed back into the pulping process. The wet CaCO_3 can be converted back to CaO by feeding it to a lime kiln, which removes its water and calcinates it, converting it to CaO and CO_2 .

2.1.2 Black liquor evaporation

Before black liquor can be burned in the recovery boiler, it is necessary to reduce its water content. Typically, black liquors exit the cooking process with dry solids mass fractions of close to 15% (Olsson, 2009). If the dry solids mass fraction in the liquor is lower than 20%, then the liquor net heating value is negative (Vakkilainen, 2007). In other words, if the liquor water content is too high, the boiler would require more heat from external sources than the amount of heat that it can produce, which would defeat the purpose.

Water content reduction is achieved by sending the black liquor to an evaporator train before it is sent to the recovery boiler. The evaporator train consists of a series of evaporator bodies through which black liquor flows and exchanges heat with low-pressure steam. Figure 2-2 is a simplified diagram illustrating the inlet and outlet vapor streams (vapor feed, vapor outlet, and condensate outlet) and the inlet and outlet black liquor streams (black liquor feed and black liquor outlet) that are part of an evaporator.

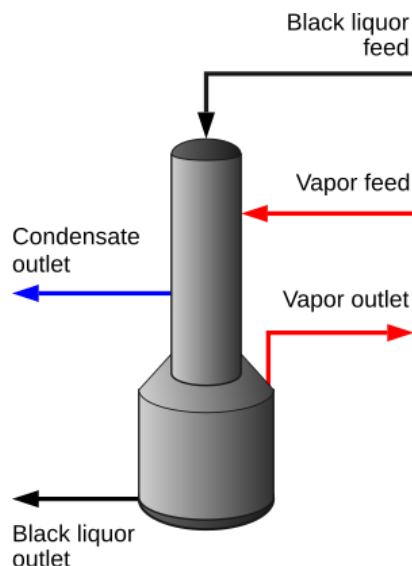


Figure 2-2: Simplified diagram of an evaporator displaying its inlet and outlet black liquor and vapor streams.

As black liquor flows through the evaporator, heat is transferred from the hotter steam to the liquor, causing steam to condense and water from the liquor to vaporize. The liquor, therefore, exits the evaporator with a higher dry solids fraction than it originally had. It is important to acknowledge that the boiling point of the liquor is higher than that of pure water. As the liquor dry solids fraction increases, so does its boiling point. This increase in the liquor boiling point temperature relative to that of pure water is quantified by the *boiling point rise* (BPR), defined as the difference between the liquor boiling temperature and the water boiling temperature measured under the same pressure (Järvinen *et al.*, 2015; da Costa *et al.*, 2016). One practical implication of the BPR is that the required steam pressure increases with the desired dry solids fraction.

Typically, there is not a single but rather multiple interconnected evaporators bodies in recovery cycle evaporator trains. The number of bodies is usually no less than five, possibly being higher than seven. Figure 2-3 depicts a typical evaporation train arrangement.

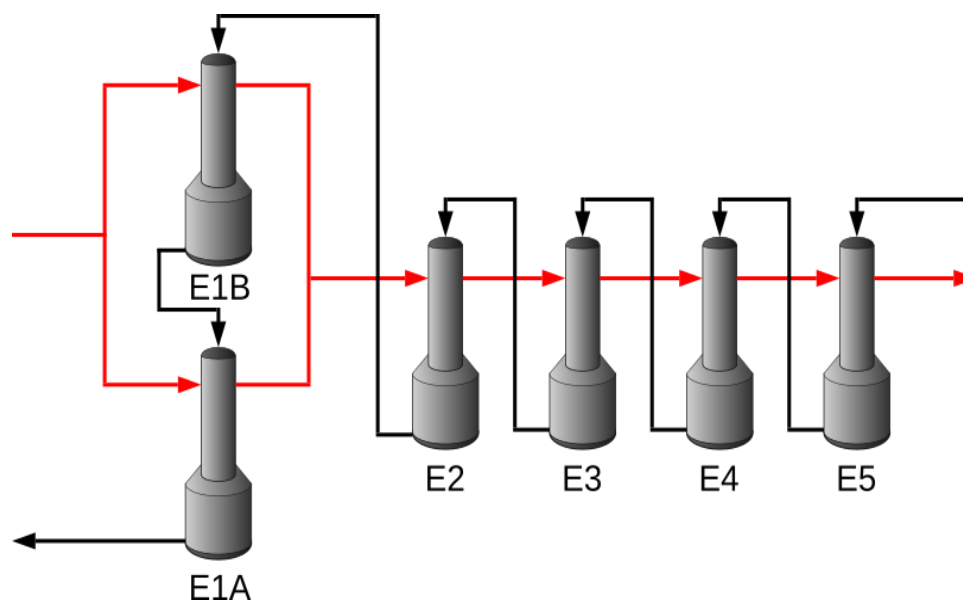


Figure 2-3: Typical arrangement of a five-effect, multiple-effect evaporator train (vapor streams are drawn in red, whereas black liquor streams are drawn in black; outlet condensate streams have been omitted for clarity's sake).

Vapor streams are drawn in red and black liquor streams are drawn in black. In this system, live steam is fed to the first two evaporator bodies, E1A and E1B. Since these two bodies operate with steam under the same pressure, they are said to be part of the same *effect*. Therefore, evaporator bodies E1A and E1B constitute the *first effect*. Heat is transferred from the live steam to the black liquor, causing water to evaporate from the black liquor along with a minor fraction of volatile organic components found in the liquor. The live steam, composed of pure water, is condensed and collected as *clean condensate* (Tikka, 2008). The vapor generated at the first effect is then fed to the second effect, composed solely of the evaporator body, E2. As before, heat exchange takes place, causing water to evaporate from the liquor and vapor to condense. This time, however, the vapor is composed of a mixture of mostly water and the volatile organic components released from the black liquor in the first effect. For this reason, this condensate is separately collected as *foul condensate* (Tikka, 2008). The same process is repeated in all subsequent effects. It is quite common to use the term *effect* in the sense just described, for which reason this type of evaporator train arrangement is usually referred to as *multiple effect evaporation* (MEE).

The goal of MEE is to increase the energetic efficiency of the system as much as possible by using part of the heat contained in the outlet vapor stream, which would otherwise be discarded, to further drive water evaporation in the subsequent effects.

2.1.3 Condensate flashing

As black liquor flows through the evaporation train, its dry solids fraction increases. In Figure 2-3, black liquor flows from right to left, which means that the dry solids concentration also increases in that same direction. During evaporation, the temperature of the vapor generated in each effect is equal to the boiling point of the liquor exiting that same effect, since they are in thermal equilibrium. That same temperature, in turn, increases with the solids fraction due to the BPR. In other words, the saturation pressure of the vapor generated in effect number i is higher than that of effect number $i+1$. This natural pressure drop along the system allows further heat to be reused by vaporizing part of the condensate and reintroducing it in the vapor line. The process by which this pressure drop is used to drive condensate vaporization is known as condensate flashing.

Figure 2-4 depicts a modified version of the previously discussed five-effect system. The condensate streams leaving effects 1 through 4 are drawn as blue lines. Condensate leaving the two bodies of the first effect are merged and sent to a clean condensate flash tank, drawn as a blue vessel. This tank is connected to the outlet vapor stream that leaves the first effect, which, as explained above, has a lower saturation pressure than that of the condensate. This pressure difference causes part of the condensate to vaporize. The vaporized fraction of the condensate then exits the flash tank and is fed to the second effect. The same logic applies to the condensates leaving effects 2 through 4. In these effects, however, foul condensate is formed. In Figure 2-4, foul condensate flash tanks are drawn as green vessels.

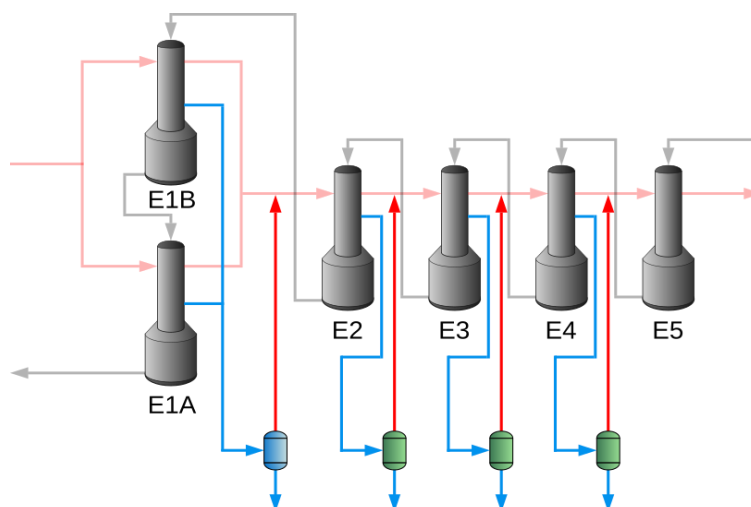


Figure 2-4: Typical arrangement of a five-effect, multiple-effect evaporator train with condensate flashing (condensate streams from effects 1–4 are drawn as blue lines, clean condensate flash tanks are drawn as blue vessels, and foul condensate tanks as green vessels).

2.1.4 Evaporator types

Evaporators vary by their design and function. In the next section, some of the most common evaporator designs are presented.

2.1.4.1 Falling film evaporators

With *falling film* (FF) evaporators, a thin film of black liquor flows downwards as a result of gravity onto a heat transfer surface, as depicted in Figure 2-5. Vapor flows on the other side of the surface, which causes heat to be transferred from the vapor to the liquor (Alhousseini, Tuzla and Chen, 1998; Chen and Gao, 2004). As the vapor loses heat, it condenses partially, causing a liquid condensate to be formed on the surface. After the black liquor reaches the bottom of the evaporator body, part of it is pumped back to the top of the evaporator, allowing it to trickle down the heat transfer surface once again. This helps maintain a relatively constant solids concentration in the evaporator, which makes it relatively insensitive to changes in the black liquor mass flow rate (Tikka, 2008). The heat transfer surface may take various geometries, such as tubular and lamellar.

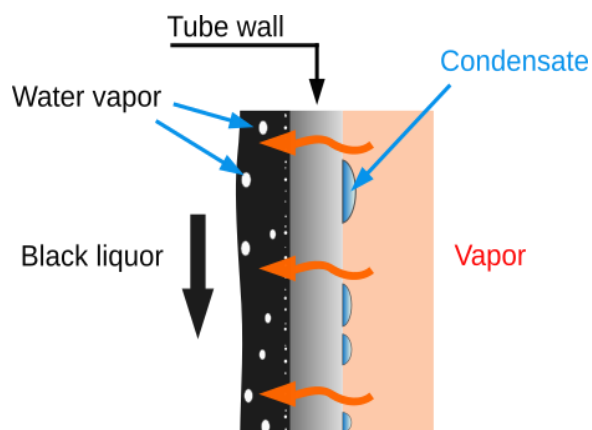


Figure 2-5: Heat transfer in a FF evaporator. Black liquor flows down the tube walls (left), while hot vapor (right) transfers heat (orange arrows) to it, causing water to evaporate. The release of heat by the vapor is accompanied by its condensation.

2.1.4.2 Rising film evaporators

Rising film evaporators, also known as *long-tube-vertical* (LTV) evaporators, were widely used in the pulp and paper industry until the mid-1980s. In modern evaporation plants, FF evaporators predominate (Tikka, 2008).

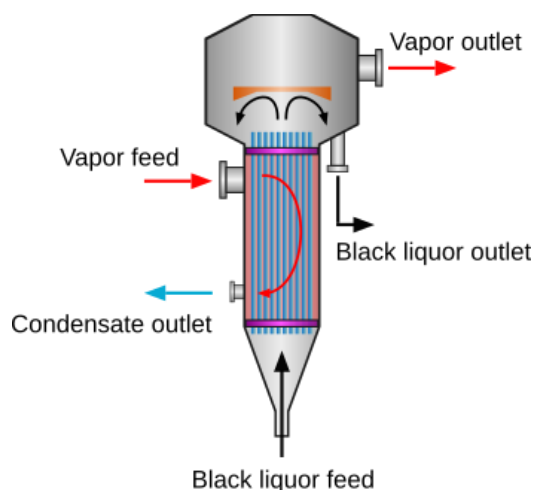


Figure 2-6: Schematic representation of a rising film (LTV) evaporator.

In this type of evaporator, black liquor is fed from its bottom and passes through an array of tubes, moving upwards, as can be seen in Figure 2-6. These tubes are usually 50 mm in diameter and have a length of about 8.5 m (Tikka, 2008). Vapor is fed to the evaporator shell and flows through the external surface of the tubes, transferring heat to the rising

black liquor and causing part of its water content to be vaporized. Having lost heat, part of the vapor condenses, and the condensate is collected below the vapor inlet. Both the vapor and the concentrated black liquor exit the evaporator from its upper shell.

If this type of evaporator is operated at low black liquor mass flow rates, the boiling of black liquor may be unstable. Moreover, low mass flow rates may lead to the generation of hotspots, which could cause scaling to occur in the tubes, leading to plugging. In this type of evaporator, plugged tubes cannot be cleaned by washing, and manual cleaning must be carried out (Tikka, 2008).

2.1.4.3 Concentrators

Concentrators are the evaporators that take the black liquor to its final desired concentration in MEE plants. Since concentrators operate at relatively high solid fractions, scaling cannot be avoided, and so concentrators need to be periodically shut down and washed (Adams, 2001; Andersson, 2015). Depending on how high a solids fraction is desired, it may be necessary to feed the concentrators with steam that is hotter than that of other evaporators. Scaling in concentrators involves the formation of burkeite and dicarbonate, both of which are double salts of sodium sulfate and sodium carbonate and can reduce the lifespan of equipment and impair their heat transfer characteristics, for which reason scaling has been the subject of several chemical characterization and modeling studies (Shi and Rousseau, 2003; Frederick *et al.*, 2004; Soemardji *et al.*, 2004; Broberg, 2012; Karlsson, Gourdon and Vamling, 2016; Karlsson, 2017).

2.1.5 Mass and energy balances in evaporators

Evaporator calculations are commonly based on performing mass and energy balances around the evaporator body (Billet and Fullarton, 1989; Tikka, 2008).

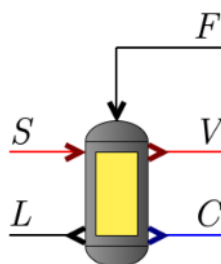


Figure 2-7: Black liquor (black), vapor (red) and condensate (blue) streams around an evaporator body.

Figure 2-7 displays the inlet (F) and outlet (L) black liquor streams, inlet (S) and outlet (V) vapor streams, and condensate stream (C) connected to an evaporator body. The inlet

vapor mass flow, \dot{m}_S , is equal to the condensate mass flow, \dot{m}_C , as the inlet vapor only undergoes condensation without any mass flow being added or removed from it, hence equation 2.1.

$$\dot{m}_S = \dot{m}_C \quad (2.1)$$

The black liquor mass flow, \dot{m}_F , entering the evaporator is split into vapor stream V having flow \dot{m}_V and concentrated liquor stream L having flow \dot{m}_L , as described in equation 2.2.

$$\dot{m}_F = \dot{m}_L + \dot{m}_V \quad (2.2)$$

Moreover, all the solids contained in stream F will be carried over to stream L , as given in equation 2.3.

$$\dot{m}_F x_F = \dot{m}_L x_L \quad (2.3)$$

Equations 2.1, 2.2, and 2.3 constitute the evaporator mass balance equations. Heat transfer is calculated by estimating the heat transfer coefficient, U , and applying it in equation 2.4:

$$\dot{Q} = UA(T_S - T_L) \quad (2.4)$$

In this equation, \dot{Q} is the transferred heat power, A is the heat transfer area, T_S is the live steam or vapor temperature, and T_L is the outlet black liquor temperature. The value of U depends on the convective heat transfer coefficient, h_{liq} , on the liquor side, on the convective heat transfer coefficient, h_{vap} , on the vapor side, and on the thermal conductivity of the heat transfer surface, k_{surf} (Costa *et al.*, 2007b, 2007a), as shown in equation 2.5:

$$U = \frac{1}{\frac{1}{h_{\text{liq}}} + k_{\text{surf}} + \frac{1}{h_{\text{vap}}}} \quad (2.5)$$

Heat transfer correlations can be calculated based on correlations that are functions of dimensionless numbers, such as Nusselt number Nu , Reynolds number Re , and Prandtl number Pr (Ding *et al.*, 2009; Johansson, Vamling and Olausson, 2009; Karlsson *et al.*, 2013; Gourdon and Mura, 2017). One such correlation is shown in equation 2.6, where C , e , and f are empirically determined constants, k is the fluid thermal conductivity, L is a characteristic length, ρ is the fluid density, μ is the fluid dynamic viscosity, v is the flow velocity, and c_p is the fluid heat capacity.

$$Nu = \frac{hL}{k} = C Re^e Pr^f = C \left(\frac{\rho v L}{\mu} \right)^e \left(\frac{c_p \mu}{k} \right)^f \quad (2.6)$$

A comprehensive list of correlations of this type has been provided by (Costa *et al.*, 2007b). It is common to use a correlation for Nu under turbulent flow and a different correlation for Nu under laminar flow. These correlations are then combined to obtain an average Nu , as shown in equations 2.7, 2.8, and 2.9 (Karlsson *et al.*, 2013):

$$Nu_{\text{lam}} = 0.882 Re^{-0.22} \quad (2.7)$$

$$Nu_{\text{turb}} = 0.0038 Re^{0.4} Pr^{0.65} \quad (2.8)$$

$$Nu = \sqrt{Nu_{\text{lam}}^2 + Nu_{\text{turb}}^2} \quad (2.9)$$

It is also possible to estimate U through other types of empirical correlations obtained from process data (Adib, Heyd and Vasseur, 2009; Khademi, Rahimpour and Jahanmiri, 2009; Chantasiriwan, 2015).

2.2 Simulation and optimization of evaporative systems

In this section, a description of the methods reported in the literature for simulating and optimizing evaporative systems is given.

2.2.1 Linear and mixed integer linear programming

Some researchers have modeled evaporative systems using linear models. This modeling strategy has the advantage of allowing for *linear programming* (LP) and *mixed-integer linear programming* (MILP) algorithms to be applied. More specifically, if an optimization can be posed as an LP, then, assuming that the problem is well posed, its global optimum can reliably and efficiently be found. On the other hand, if the problem is posed as an MILP, it is still the case that the global optimum can be reliably found, but the efficiency may suffer, since MILP algorithms usually rely on some type of branch-and-bound strategy (Luenberger, Ye and others, 2010).

Ji and collaborators (2012) attempted to optimize the energy cost of a pulp and paper mill subsystem comprised of a digester and an evaporation plant using LP. The model was solved using the commercial package CPLEX, which can solve both LP and MILP problems (Ji *et al.*, 2012). In this study, the authors used data collected from an operating pulp and paper mill, whose evaporator plant structure is shown in Figure 2-8, to construct a linear Excel® model that correlated the outlet steam mass flow with other inlet steam and black liquor variables. The model is shown in in equation 2.11:

$$f_{steam} = -0.6897 TS\%_{in} - 0.552t_{in} + 0.8655f_2 - 0.4288t_3 + 0.2445 TS\%_{in} + 0.1182f_{in} \quad (2.10)$$

In this equation, the terms of form $TS\%$ refer to the black liquor dry solids mass fraction, those of form f refer to mass flow rates, and those of form t refer to temperatures in °C. The subscripts refer to the streams to which they pertain. These streams can be found in Figure 2-8.

From an optimization standpoint, equation 2.10 acts as an equality constraint. The objective function to be minimized, which represents cost, is given in equation 2.11:

$$f_{obj} = c_{oil}m_{oil} + c_{bark}m_{bark} + c_{el,purchased}q_{el,purchased} - c_{el,produced}q_{el,produced} \quad (2.11)$$

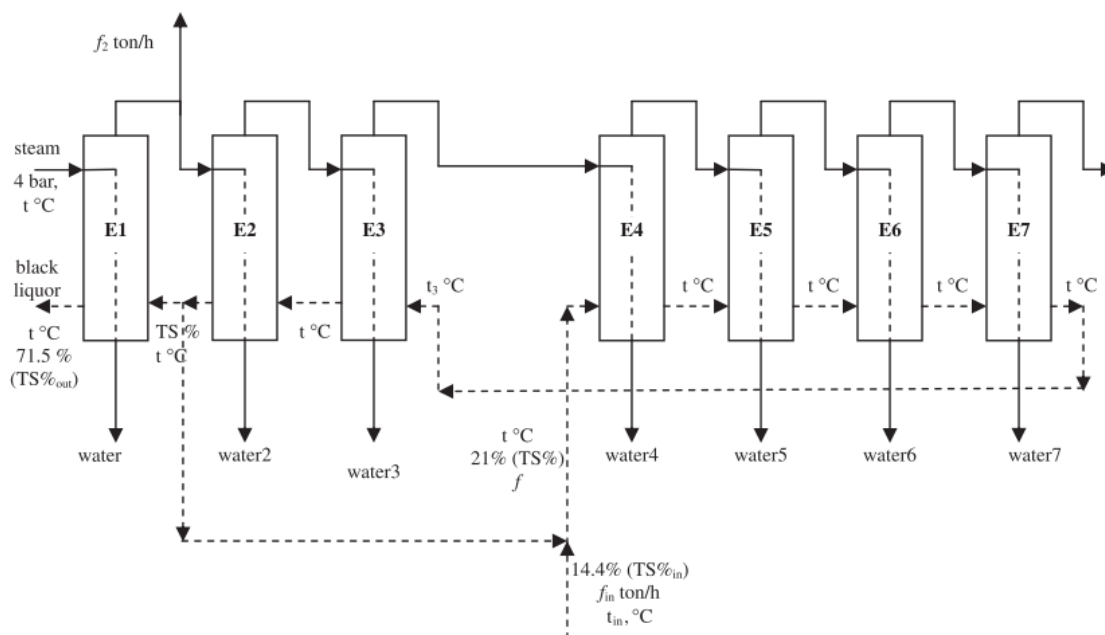


Figure 2-8: Seven-effect evaporation plant optimized by (Ji *et al.*, 2012) using linear optimization techniques (derived from (Ji *et al.*, 2012)).

In this equation, c_{oil} , c_{bark} , $c_{el,purchased}$ and $c_{el,produced}$ represent, respectively, the oil cost €/ton, bark cost in €/ton, electricity cost in €/MWh, and electricity revenue when electricity is sold (negative cost) in €/MWh. The terms of form m denote mass in tons, whereas terms of form q denote energy in MWh.

The authors found that the model was useful for testing different operational scenarios for the pulp mill under study. It should be noted, however, that this type of study is a process-specific study, and that the values reported for this process may not be interchanged with others.

A more sophisticated and more general study focusing on MILP was conducted by Kermani and collaborators (2016). In this study, the authors developed a MILP-based process integration methodology for simultaneously optimizing water and energy consumption in a Kraft pulping mill (Kermani *et al.*, 2016). Also worth mentioning is a study by Khanam and Mohanty (2010), where they proposed energy reduction schemes for MEE systems (Khanam and Mohanty, 2010). Their study involved enumerating a collection of possible evaporator arrangements.

The authors, starting from nonlinear heat exchanger models, generated new linearized models following a methodology similar to that described by Floudas (2006) in his seminal text *Deterministic Global Optimization*, where nonlinear terms are replaced by linear terms and extra constraints are added to the complete optimization problem

(Floudas, 2013). Once the models were linearized, the complete optimization problem was formulated as an MILP closely following the methodology described by Biegler and collaborators (1997) for pinch analysis (Biegler, Grossmann and Westerberg, 1997). Another noteworthy, albeit less mathematically sophisticated, linear approach to process integration is the one described by Mesfun and Toffolo (2015). In their study, the authors carried out the process integration of an entire Kraft pulp mill using pinch analysis (Mesfun and Toffolo, 2015). A simple but general linear optimization method has also been described by Kaya and Sarac (2007) for optimizing a four-effect, parallel-flow evaporator plant in terms of energy economy (Kaya and Ibrahim Sarac, 2007).

2.2.2 Nonlinear programming

From a phenomenological standpoint, the modeling of evaporative systems rests on mass and energy balances. The latter naturally introduces nonlinearities into the models, which accounts for the large number of nonlinear models among those reported in the literature. A comprehensive review of these methods has been given by (Verma, Manik and Sethi, 2019).

Bhargava and collaborators (2008) modeled the MEE system displayed in Figure 2-9 using phenomenological equations corresponding to mass and energy balances. This MEE system is particularly important because it served as a basis for the work of subsequent researchers, such as Jyoti and Khanam (2014). The model was built using both linear equations, global mass balances, and nonlinear equations, solids balances and energy balances.

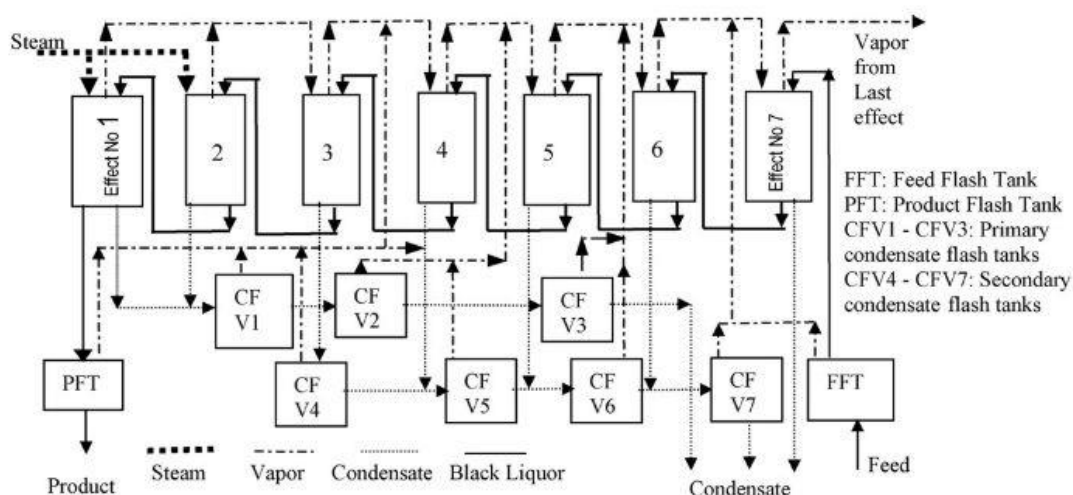


Figure 2-9: Seven-effect MEE system studied by Bhargava and collaborators (derived from (Bhargava *et al.*, 2008).

The authors manually tried different black liquor flow patterns for this system to find the one that maximized steam economy, that is, the ratio between the total vapor generated in the MEE plant and the amount of live steam supplied to it. Figure 2-10, derived from their original publication, shows the different arrangements that were tried. In this figure, **F** denotes the sequence of effects through which black liquor flows.

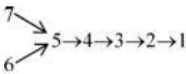
Seq. no.	F	Remarks
a	7 → 6 → 5 → 4 → 3 → 2 → 1	Backward F, feed to seventh effect
b		Backward F, feed splits equally among sixth and seventh effects
c	6 → 7 → 5 → 4 → 3 → 2 → 1	Mixed F, feed to sixth effects
d	5 → 6 → 7 → 4 → 3 → 2 → 1	Mixed F, feed to fifth effect
e	4 → 5 → 6 → 7 → 3 → 2 → 1	Mixed F, feed to fourth effect
f	3 → 4 → 5 → 6 → 7 → 2 → 1	Mixed F, feed to third effect

Figure 2-10: Black liquor flow patterns studied by Bhargava and collaborators (E derived from (Bhargava *et al.*, 2008).

Jyoti and Khanam (2014) modeled the MEE system displayed in Figure 2-11 in a similar way as Bhargava and collaborators. The model was solved using a non-specified iterative procedure. The authors then manually experimented with different numbers of flashing tanks and vapor bleeding strategies to find the most economical arrangement, as measured by cost function.

Mesfun and Toffolo (2013) carried out process integration of a combined heat and power (CHP) system and the evaporator plant at a Kraft mill. Their process integration approach was based on pinch analysis and used an evolutionary algorithm called the Genetic Diversity Evaluation Method (GeDEM). The authors claimed that this evolutionary algorithm was chosen due to its robustness to withstand potentially large variations in the calculated values for the pinch-point temperatures. By manually changing the MEE system configuration, the authors were able to identify energy-saving opportunities.

Another interesting study involving MEE process integration is one by Sharan and Bandyopadhyay (2016), where they used models quite similar to those used by Bhargava and collaborators (2008) to model an evaporator train for a desalination system. It is worth noting that despite the fact that the present dissertation focuses on Kraft MEE plants, the models used to describe them can be modified to fit the needs of other industries. Diel and collaborators (2016) optimized a MEE system by generating response surfaces and then subjecting these surfaces to statistical analyses. Their methodology involved solving a nonlinear system of equations several times.

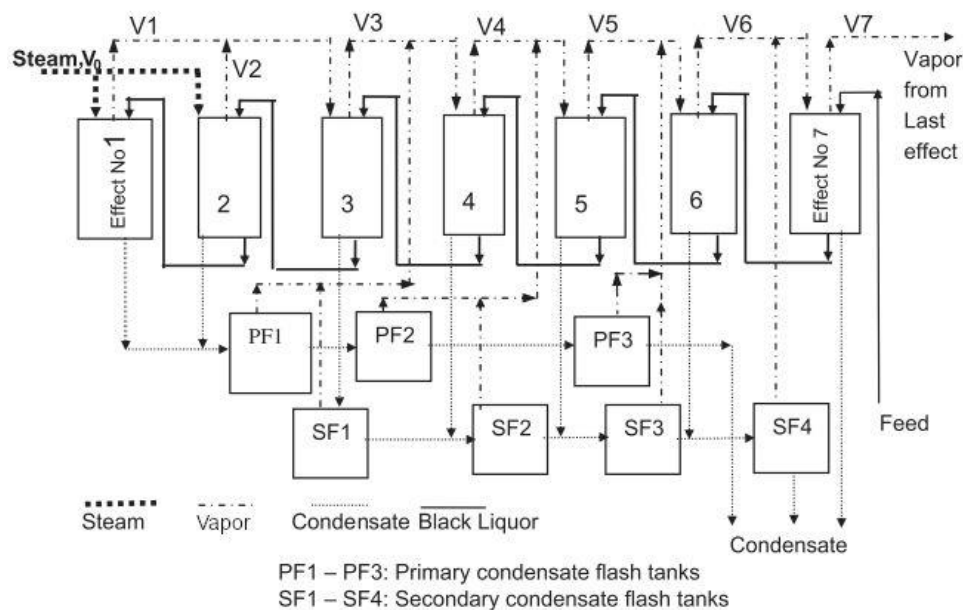


Figure 2-11: Seven-effect MEE system studied by Jyoti and Khanam (adapted from (Jyoti and Khanam, 2014)).

Olsson (2009b) developed a simulation tool called OptiVap for simulating MEE systems and used it to optimize MEE systems that account for lignin extraction and the use of excess heat.

2.3 General process simulation techniques

The methods described in the preceding section are best used for modeling evaporative systems that have a fixed *topological structure*. The term topological structure refers to the number of evaporator bodies, or any other unit processes, in a system and the way in which they are interconnected. Notice that, by following the above-mentioned methodologies, if a system were to change its structure, the equations that describe it would then have to be changed as well. These methodologies, for this reason, would have trouble describing a system whose structure is either unknown or dynamic.

More general methodologies, which can accommodate a variety of process structures, have been thoroughly studied and reported in the chemical engineering literature, and it is due to them that a variety of general-purpose process simulators are available today.

Process simulators are commonly used in the pulp and paper industry to facilitate the analysis and flowsheeting of evaporator plants. Cardoso and collaborators (2009) used the commercial simulator WinGEMS along with continuous data collected from a Brazilian pulp mill to identify opportunities for saving energy. In their work, continuous online data from a six-effect evaporation plant was fed to WinGEMS, which then calculated the heat transfer coefficient of each evaporator body in the plant (Cardoso *et*

al., 2009). The MEE plant is depicted in Figure 2-12. By analyzing how these calculated coefficients varied, it was possible to schedule a washing routine for the evaporators, which optimized their energy use.

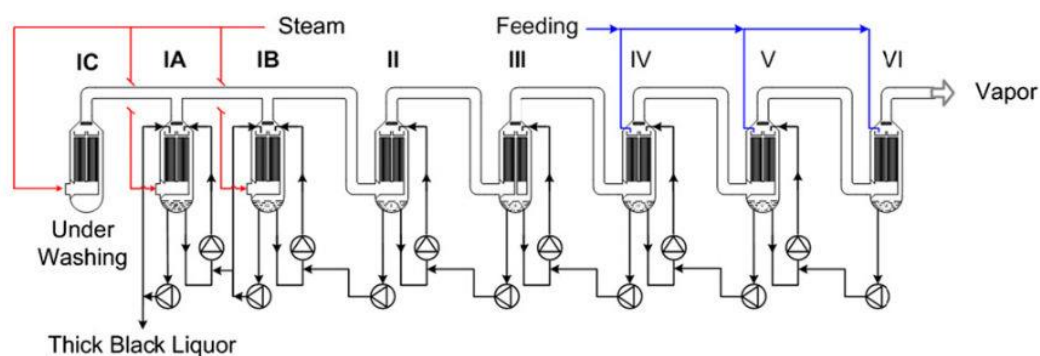


Figure 2-12: Six-effect MEE train from a Brazilian pulp mill studied by Cardoso and collaborators (derived from (Cardoso *et al.*, 2009).

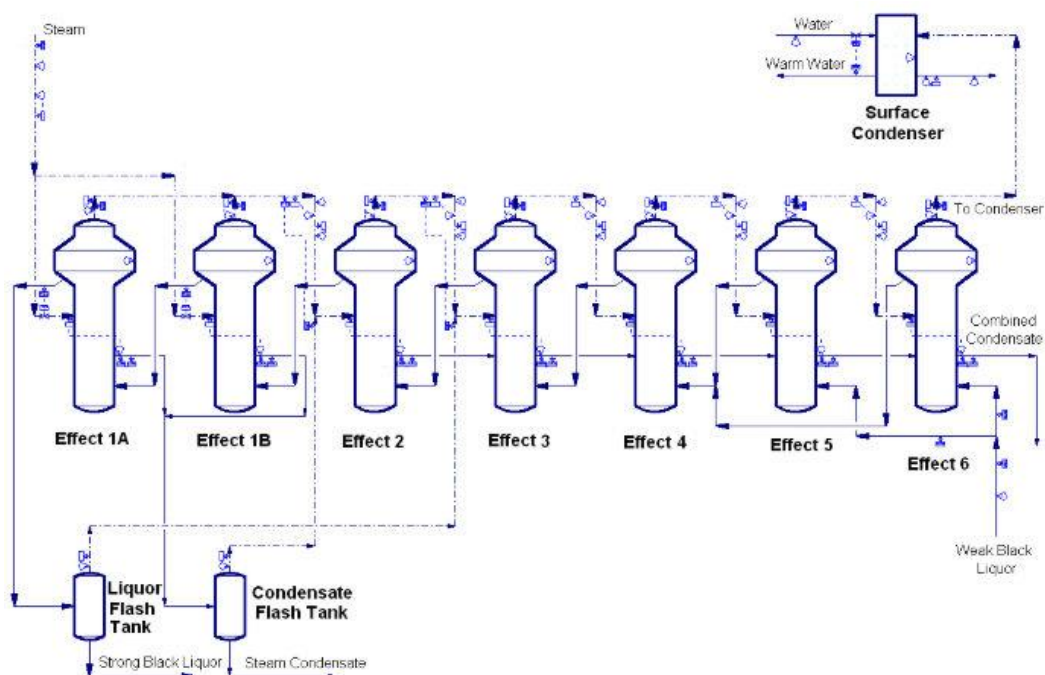


Figure 2-13: ChemCAD diagram of a six-effect MEE train studied by Saturnino (adapted from (Saturnino, 2012).

Saturnino (2012) calculated the chemical balance of an entire Kraft pulp mill as part of doctoral research, a procedure that involved calculating its evaporation plant, displayed

in Figure 2-13. He performed the MEE evaporator calculation with the aid of two process simulators, WinGEMS and ChemCAD, and then compared the results (Saturnino, 2012). Satisfactory agreement was found between the results obtained from both simulators.

General process simulation methodologies are commonly divided into two broad categories, namely an *equation-oriented approach* (EOA) and *sequential-modular approach* (SMA) (Westerberg *et al.*, 1979). It should be noted, however, that some methodologies combine aspects of both EOA and SMA.

The hypothesis posed in this dissertation is that there exists a methodology through which it is possible to optimize evaporator systems both with respect to their topological arrangement and other internal design variables. If this is the case, the methodology must contain in its core a set of subroutines that allow for systems of general topological complexity to be simulated. In principle, both EOA and SMA simulation approaches can do so, which motivated their use in this dissertation.

Of course, it remained to be seen whether these methodologies would have good convergence properties for the systems that were studied. Another question would be that of selecting an optimization procedure that would work well alongside the simulation procedure. In the next sections, the EOA and SMA approaches are described in more detail, and an overview of mathematical optimization methods is given.

2.3.1 Sequential-modular approach

With the sequential-modular approach, each unit process of a system is abstracted as an independent module. The mass and energy flows that are transferred between the unit processes are abstracted as process streams, which interconnect the modules. Each module is responsible for calculating the properties of its outlet streams given its module parameters and the properties of its inlet streams. Figure 2-14 shows a system consisting of three process modules, here represented by rectangular blocks, and six streams, represented by arrows. In this example, each module is connected to two input streams and two output streams.

If the properties of the leftmost process streams are known, module 1 can be executed to calculate the properties of its two output streams. These streams serve as input for module 2. Since their properties are now known, module 2 can be executed to calculate its outlet streams. These, in turn, serve as inputs for module 3. Upon executing block 3, the rightmost streams can finally be calculated. The properties of all streams can thus be determined by executing the modules in a certain order, in this example 1–2–3. Notice that the calculation order is tightly related to the topology of the process being analyzed.

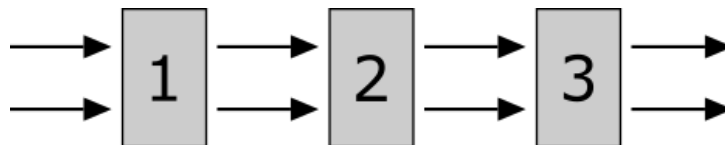


Figure 2-14: Calculation of a process model using a SMA methodology. The process topology suggests that the modules should be calculated in the order of 1–2–3.

In practical systems, however, it is quite common to find topologies such as the one shown in Figure 2-15(a). Notice that the blue stream serves as input for module 1 and as output for module 3. This topological feature is commonly known as a *recycle*, for which reason the blue stream is referred to as a *recycle stream*. In this case, the calculation is not as straightforward as before since the calculation for module 1 requires information that can only be obtained by calculating module 3. Module 3, on the other hand, depends on the outputs of module 1.

In this case, an iterative procedure must be carried out. In Figure 2-15(b), the recycle stream has been *torn*. In the procedure known as *stream tearing*, recycles are eliminated by breaking recycle streams into pairs of independent streams (Westerberg *et al.*, 1979; Mah, 2013). The calculation sequence in this example begins with an initial estimate of the properties of the torn stream. Module 1 can be executed based on this initial estimate, followed by modules 2 and 3. The result from module 3 will yield new property values for the torn stream, which will, in general, be different than the initial estimate. Based on these new values, the torn stream properties can be updated. This process is repeated until the difference is sufficiently small. This procedure is sometimes referred to as *converging the recycles*.

Several methods have been described in the literature for tearing recycle streams as well as for converging recycles. Common algorithms for recycle convergence are fixed-point iteration, Wegstein's method, and the NR method (Smith, 2016).

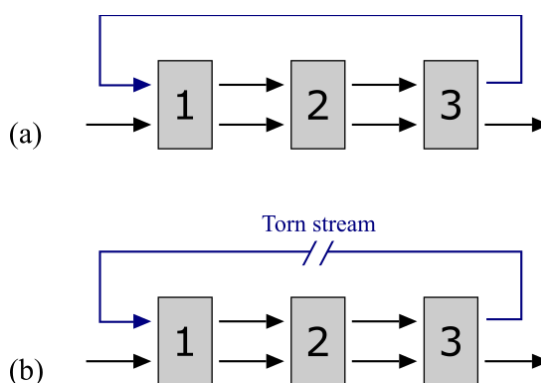


Figure 2-15: Stream tearing procedure in an SMA simulator.

2.3.2 Equation-oriented approach

Generally speaking, as the number of recycles in a system increases, the harder and slower it will be for SMA methods to converge, since more initial estimates need to be provided and more iterations will be necessary for convergence to be achieved. An alternative methodology that may facilitate convergence is the equation-oriented approach.

With this approach, each unit process is abstracted as a set of equations. Figure 2-16 displays a process flowsheet composed of three unit processes. Let \mathbf{x} be a vector containing all process variables necessary to calculate this flowsheet. In this example, process 1 is described by the equations $f_1(\mathbf{x})$ and $f_2(\mathbf{x})$, process 2 by $g_1(\mathbf{x})$ and $g_2(\mathbf{x})$, and process 3 by $h_1(\mathbf{x})$ and $h_2(\mathbf{x})$. These equations are collected and assembled into a *global system of equations* (GSOE). The GSOE can then be solved using any of the many available numerical methods for solving systems of linear and nonlinear equations. Notice, however, that these methods require initial estimates for the variables to be provided. The quality of these estimates will determine how well the algorithms will converge.

Notice that the topological structure of the process is disregarded in EOA: the interconnectivity between the block no longer dictates the calculation order. If good initial estimates can be provided, this may greatly facilitate the convergence of systems with many recycles. The GSOE solution can be further facilitated by examining the dependences between its equations and variables. Equations that, for instance, only depend on a single variable can be solved first.

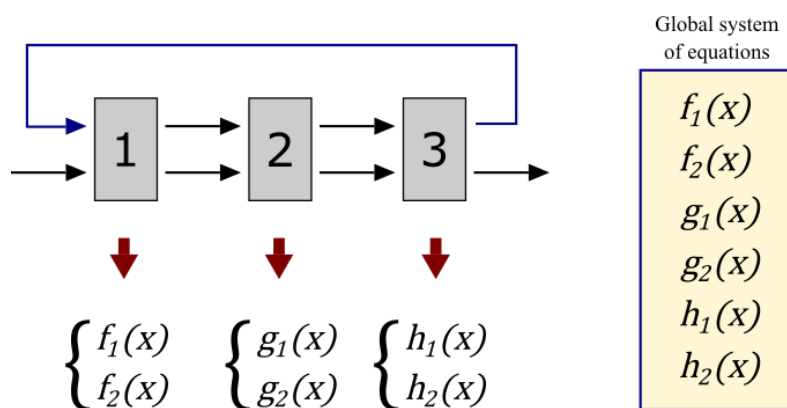


Figure 2-16: Calculation of a process model of an EOA methodology. Each process module contributes a set of equations that make up an overall general system of equations (GSOE).

2.4 Mathematical optimization

2.4.1 General aspects

A general mathematical optimization problem can be written as follows (Floudas, 2013):

$$\begin{aligned} \min \quad & f(\mathbf{x}) \\ \text{s. t.} \quad & h_i(\mathbf{x}) = 0 \\ & g_j(\mathbf{x}) \leq 0 \end{aligned} \tag{2.12}$$

In this type of problem, a vector of scalars denoted by \mathbf{x} is sought such that it minimizes the value of the objective function, here denoted by f , evaluated at \mathbf{x} , while satisfying the equality and inequality constraints represented by equations h_i and inequalities g_j , respectively.

An optimization problem may be either *constrained* or *unconstrained*. A constrained problem contains at least one equality or inequality constraint, whereas none are present in an unconstrained problem.

A vast number of engineering problems can be modeled as mathematical optimization problems (Boyd and Vanderberghe, 2004; Floudas, 2013). Problems involving cost minimization are a natural fit.

Finding a solution to the general problem expressed by equation 2.12 is not trivial. This is due to the general formulation-accommodating functions, which may be ill-behaved or contain local minima. A *local minimum* is a point whose objective function value is lower than that of those in its neighborhood. If its value is also lower than that of every other point in the function domain, then it is also said to be the *global minimum*. Figure 2-17 displays a function with a local minimum at point (5,6) and a global minimum at point (3,3).

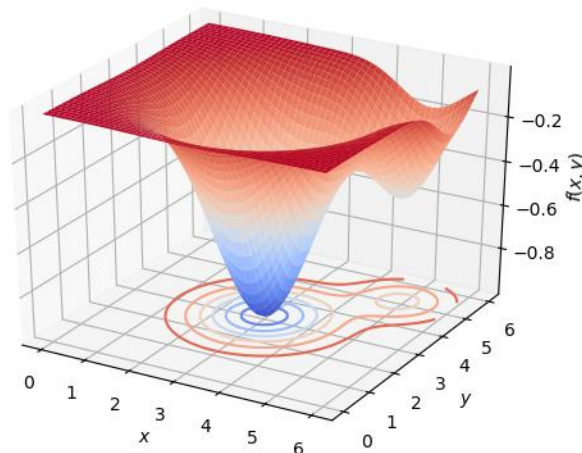


Figure 2-17: Graph of a function displaying a global minimum at point (3,3) and a local minimum at point (5,6).

In many cases, such as in costs optimization, it is highly desirable to find the global minimum. The existence of local minima is an obstacle to optimization in these cases, since the algorithms usually applied to solve them are prone to being trapped in local minima. This situation can be remedied by either re-running the algorithm with new initial estimates or by trying new algorithms. A brief overview of the types of algorithms usually applied in practice is given in the following section.

2.4.2 Deterministic algorithms

Optimization algorithms are iterative and can be divided into two broad categories: deterministic and stochastic. Deterministic algorithms are guaranteed to execute the same sequence of steps every time. These algorithms usually depend on the user providing an initial estimate for the values of the choice variables. This initial estimate is then updated at each iteration until it either meets a predetermined convergence criterion or until a maximum number of iterations is reached. The quality of this initial estimate determines whether the algorithm will converge, how close it will get to the actual solution, and how many iterations are needed for it to halt.

Since deterministic algorithms depend on the quality of the initial estimate, they are susceptible to converging to local minima, or to not converging at all. Even still, these algorithms tend to converge quickly with a high degree of precision if the problem under study is convex (Boyd and Vanderberghe, 2004), or if high-quality initial estimates can be provided. Important exceptions to the initial estimate requirement are the standard algorithms used for solving linear programming problems, that is to say, optimization problems whose objective function and constraints are linear. Such algorithms as the simplex method or interior point method have a built-in subroutine for generating initial

estimates that converge, for which reason they are, in practice, preferred (Luenberger, Ye and others, 2010).

Deterministic algorithms for nonlinear optimization problems may be classified with respect to the order of the derivatives required during their execution. For instance, if no derivatives are required by the algorithm, it is said to be a zero-order method. Likewise, if at most the first derivative of the objective function and constraints are required, it is classified as a first-order method. Algorithms that require second derivatives are, finally, classified as second-order methods (Price, Storn and Lampinen, 2005; Luenberger, Ye and others, 2010).

Zero-order methods are useful for optimizing problems whose functions are either discontinuous or whose first derivative is ill-behaved. Examples of such algorithms are the Hooke-Jeeves method and the Nelder-Mead method (Price, Storn and Lampinen, 2005). Variants of these two algorithms are currently being implemented in scientific computing packages such as MATLAB® (‘MATLAB Optimization Toolbox’, 2018). These algorithms usually function by sampling points in the neighborhood of the current estimate at each iteration and updating the estimate using the objective function values at these points.

First-order methods use the objective function’s first derivative to iteratively update the initial estimate, ideally bringing it closer to the minimum point. A well-known first-order algorithm for unconstrained nonlinear problems is the gradient descent method. With this method, the objective function gradient is calculated either analytically or numerically at each iteration, and the current estimate is moved in the direction opposite to that of the gradient, as shown in equation 2.13.

$$\mathbf{x}_{n+1} = \mathbf{x}_n - \alpha_n \nabla f(\mathbf{x}_n) \quad (2.13)$$

In this equation, \mathbf{x}_n is the estimate for the minimum at the n^{th} iteration and α_n is a step-control parameter, which is a positive number that may either depend on the current iteration or remain constant. If α_n is taken as a sufficiently small value, it can be shown that \mathbf{x}_{n+1} is guaranteed to be less than \mathbf{x}_n (Luenberger, Ye and others, 2010). Even though smaller values of α_n favor convergence, they also tend to increase the number of iterations necessary for the algorithm to converge.

Second-order methods use the first and second derivatives of the objective function and constraints. The canonical example is the Newton-Raphson (NR) method, shown in equation 2.14.

$$\mathbf{x}_{n+1} = \mathbf{x}_n - \alpha_n \mathbf{H}^{-1}(\mathbf{x}_n) \nabla f(\mathbf{x}_n) \quad (2.14)$$

In this equation, $\mathbf{H}^{-1}(\mathbf{x}_n)$ denotes the inverse Hessian matrix of the objective function evaluated at \mathbf{x}_n , where the Hessian is defined elementwise as $[\mathbf{H}]_{ij} = \left. \frac{\partial^2 f}{\partial x_i \partial x_j} \right|_{\mathbf{x}_n}$ and α_n is a positive step-control parameter. The NR method converges remarkably quickly when a good enough initial estimate is provided. This property, more properly stated, is known as *quadratic convergence* (Luenberger, Ye and others, 2010). Despite this attractive property, the NR method is still susceptible to being trapped in local optima, and, in practice, numerically evaluating the Hessian matrix at each iteration may be prohibitively costly since the number of entries in that matrix increases quadratically with the number of variables. In other words, the NR method may actually be too computationally heavy to be used in larger problems. It should be noted that equation 2.14 is not implemented as it is in robust computational packages, since this equation involves inverting the Hessian and then multiplying it by the gradient. It is instead more efficient to solve the linear system shown in equation 2.15, which is equivalent to the former equation (Boyd and Vanderberghe, 2004).

$$\mathbf{H}(\mathbf{x}_n)(\mathbf{x}_{n+1} - \mathbf{x}_n) = \nabla f(\mathbf{x}_n) \quad (2.15)$$

A family of algorithms known as Quasi-Newton was developed to combine the NR method's rapid convergence rate, while remedying its scalability issues for large problems. The Broyden-Fletcher-Goldfarb-Shanno method, abbreviated as BFGS, belongs to this family and is commonly implemented in scientific packages. It proceeds very much like the NR method, but instead of recalculating the Hessian every iteration, it is instead updated using *rank one updates* (Luenberger, Ye and others, 2010).

$$\begin{aligned} \mathbf{B}_n \mathbf{p}_n &= \nabla f(\mathbf{x}_n) \\ \mathbf{s}_n &= \alpha_n \mathbf{p}_n \\ \mathbf{x}_{n+1} &= \mathbf{x}_n + \mathbf{s}_n \\ \mathbf{q}_n &= \nabla f(\mathbf{x}_{n+1}) - \nabla f(\mathbf{x}_n) \\ \mathbf{B}_{n+1} &= \mathbf{B}_n + \frac{\mathbf{q}_n \mathbf{q}_n^T}{\mathbf{q}_n^T \mathbf{s}_n} - \frac{\mathbf{B}_n \mathbf{s}_n \mathbf{s}_n^T \mathbf{B}_n}{\mathbf{s}_n^T \mathbf{B}_n \mathbf{s}_n} \end{aligned} \quad (2.16)$$

The formulae displayed in equation 2.16 show the steps involved in the BFGS method. The matrix \mathbf{B} is an approximation of the much slower to calculate Hessian matrix, and it is updated at each iteration and then used to calculate a step size, \mathbf{s}_n , controlled by the step-control parameter α_n . Depending on the implementation, \mathbf{B} may be initially set to the identity matrix or made equal to the Hessian matrix evaluated at the initial estimate, \mathbf{x}_0 . The term rank one refers to the outer vector products of the form, $\mathbf{q}_n \mathbf{q}_n^T$, which are matrices with a rank equal to one since all its columns are multiples of each other. Due to this unique characteristic of rank-one matrices, matrix operations involving them can be optimized, thus making the algorithm more efficient.

2.4.3 Stochastic algorithms and differential evolution

Stochastic algorithms involve randomness in their execution, for which reason the sequence of steps taken during their execution is not guaranteed to be the same. In fact, it is their very randomness that helps them overcome, to some extent, a major difficulty faced by deterministic algorithms, that is, the presence of local minima.

Differential evolution (DE) is an evolutionary algorithm that has found wide acceptance in multiple fields of knowledge and is particularly well suited for global optimization over continuous spaces (Price, Storn and Lampinen, 2005). It has been successfully applied in the optimization of a wide variety of energy optimization systems, from heat exchangers to wind farms (Afanasyeva *et al.*, 2013; Saari *et al.*, 2014, 2019). The implementation details are given below.

Initially, a population of N_p D -dimensional vectors is randomly generated, where D is the number of choice variables of the problem under study. Each one of the vectors will be denoted by \mathbf{x}_i , where i ranges from 0 to $N_p - 1$. This population will be referred to as the first *generation* of vectors.

It is necessary that the user supplies upper and lower bounds for each one of the choice variables to be initialized for DE. Let \mathbf{x}_i be a population vector and let $x_{i,j}$ denote its j^{th} variable. Let b_j^L and b_j^U be the lower and upper bounds corresponding to the j^{th} variable. Each variable is then uniformly sampled according to equation 2.17:

$$x_{i,j} = b_j^L + \text{rand}(0,1)(b_j^U - b_j^L) \quad (2.17)$$

Once all variables of all N_p vectors are uniformly sampled, the *initialization step* is complete. The algorithm now proceeds to the *mutation step*.

During mutation, N_p mutant vectors \mathbf{v}_i , also known as *target vectors*, are generated by adding a random, scaled difference between two randomly chosen vectors, \mathbf{x}_1 and \mathbf{x}_2 , to a third one, \mathbf{x}_0 . It is important that all three vectors are distinct from each other, meaning that no vector is sampled more than once. Vector \mathbf{x}_0 is known as the *base vector*, whereas \mathbf{x}_1 and \mathbf{x}_2 are the *difference vectors*. In the basic DE implementation, \mathbf{x}_0 is randomly selected, while taking care that its index in the population is not equal to the target vector's index. Other implementations of DE, however, might follow a different strategy. In fact, other implementations might even add more than one scaled difference to the base vector (Price, Storn and Lampinen, 2005).

$$\mathbf{v}_i = \mathbf{x}_0 + F(\mathbf{x}_1 - \mathbf{x}_2) \quad (2.18)$$

Here, F is known as the scale factor, which can, in theory, take any positive value. In practice, however, it is seldom the case that F takes values much higher than one (Price, Storn and Lampinen, 2005).

Next, DE enters the crossover step, where the original and target vectors are interleaved to the extent determined by the crossover probability, CR . Intuitively, this means that the vectors are being shuffled, which helps to reduce the likelihood of the algorithm getting trapped in a local optimum. A collection of N_p trial vectors \mathbf{u}_i is constructed as follows. For every $i \in 0, \dots, N_p - 1$, initialize \mathbf{u}_i as an empty vector and uniformly select a variable index, $j_{rand} \in 0, \dots, D - 1$. Take the corresponding original and target vectors, \mathbf{x}_i and \mathbf{v}_i , and copy their values to \mathbf{u}_i as follows: for each component $j \in 0, \dots, D - 1$, uniformly sample a random number r between 0 and 1. If $r \leq CR$, or if $j = j_{rand}$, copy $v_{i,j}$ into $u_{i,j}$. If that is not the case, copy $x_{i,j}$ into $u_{i,j}$. Notice that if $j = j_{rand}$, then the trial vector is guaranteed to receive data from the target vector. This is done to ensure that trial vector \mathbf{u}_i is not a duplicate of \mathbf{x}_i (Price, Storn and Lampinen, 2005).

Lastly comes the selection stage. Here, DE checks whether each of the generated trial vectors, \mathbf{u}_i , resulted in a lower objective function value when compared to the corresponding original vector, \mathbf{x}_i . If that is the case, \mathbf{u}_i replaces \mathbf{x}_i in the next generation. Once this check is made for all trial vectors, DE loops back to the mutation stage and the process is repeated until either a convergence criterion is met or the maximum number of generations is exceeded.

The method just described is referred to by the original authors as Classic DE, or rand/1/bin. The latter notation, which is useful for describing variations of this method, states that during the mutation step, the base vector is randomly selected and then added to one scaled vector difference. In the crossover step, the components, j , of the trial vector are selected from either \mathbf{x}_i or \mathbf{v}_i , a process controlled by the crossover probability, CR . This approximates a Bernoulli process with probability CR , the only difference being that if $j = j_{rand}$, then $v_{i,j}$ is copied to $u_{i,j}$ regardless of CR . Since the crossover step is approximated by a sequence of D independent Bernoulli steps, the probability distribution

of the components of \mathbf{u}_i approximates a binomial distribution (Feller, 1957; Price, Storn and Lampinen, 2005).

Figure 2-18 provides a visual representation of how DE progresses when optimizing a function with two local minima. At generation zero, the population vectors, represented by black dots, are uniformly scattered throughout the domain. As the number of generations increases, the vectors cluster together close to the optima, eventually migrating to the global optimum.

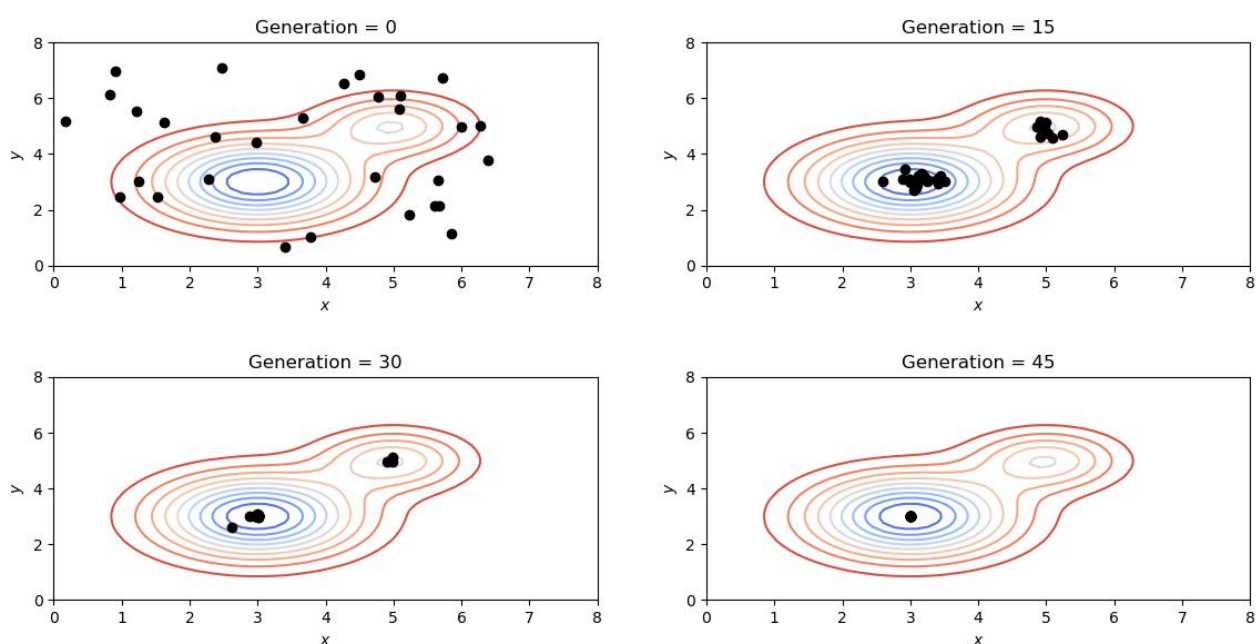


Figure 2-18: Optimizing a function with local optima using DE (the colored curves are the function's contour lines and the black dots are the vectors corresponding to each generation).

DE is parameter-dependent: the user needs to supply the number of vectors in the population, Np , the scaling factor, F , and the crossover probability, CR . These numbers can be determined by running DE with different combinations thereof, a procedure known as *parameter tuning*.

Low values of F and Np accelerate convergence, but at the same time they increase the likelihood of convergence at a local optimum. As a rule of thumb, it is often recommended to set $Np = 10D$ (Storn, 1996; Price, Storn and Lampinen, 2005). If D is very high, (Ghosh *et al.*, 2017) recommend setting $Np = 0.1D$. As for F , an initial estimate of $0.7 \leq F \leq 0.9$ is often recommended (Ronkkonen, Kukkonen and Price, 2005; Yang, 2010), even though lower (Gämperle, Müller and Koumoutsakos, 2002) and higher (Ghosh *et al.*, 2017) values have also been suggested.

3 Methodology

The research hypothesis of this dissertation is that there exists a methodology for simultaneously optimizing evaporation systems with respect to their structure and to their internal variables. It is also important to assess how well it converges and scales for larger problems.

The optimization algorithm chosen for this type of problem was Differential Evolution, due to its reported success in optimizing a wide variety of problems, as well as due to it being particularly well suited for global optimization over continuous spaces (Price, Storn and Lampinen, 2005).

Another reason for the choice of DE was the fact that each objective function evaluation corresponds to solving an entire MEE flowsheet, which is a computationally heavy operation. Other methods, such as those of the quasi-newton family would require many more function evaluations per iteration, which would sharply increase the computational load required for optimization, thus hindering it from being applied in practice. Another advantage of DE is the fact that its stochastic nature makes it less likely to become trapped at a global optimum.

In this dissertation, the research hypothesis is proved by presenting a general methodology for performing the topological optimization of MEE systems. At its core, the methodology depends on a simulation engine that makes it possible to model and simulate the MEE systems of arbitrarily complex structures.

Manually coding complex systems is a tedious and error-prone process. Assembling MEE flowsheets can be greatly facilitated by exposing the user to a graphical user interface (GUI), through which it is possible to assemble the block diagram corresponding to the MEE system under study and to input process parameters.

Taken as a whole, the GUI and the simulation engine constitute a complete steady-state MEE EOA simulator. The simulator engine was initially written in MATLAB. Once the calculation procedures were shown to yield good results, the engine was rewritten in C++, and a GUI written in Python 3.8 was added.

After the EOA simulator was built and tested, a new SMA engine was built and integrated with the same GUI. Switching engines was relatively straightforward, as the communication between GUI and engine was done using an application-programmer interface (API) based on the ubiquitous file format known as JSON, which helped to uncouple these two software components.

In the following sections, the architecture of both the EOA and SMA simulation engines are described. Immediately after these sections, a description of the evaporator model chosen for this dissertation, as well as a simplified version thereof, are given. This is

followed by a description of calculation procedures utilized for physical properties estimation of water vapor and black liquor.

Next, the validation procedure for the evaporator model is described. In this step, data taken from the literature was used to gauge how well the model performed. Once the model results were considered sufficiently good, the topological optimization of two MEE systems was carried out. This is described immediately after the model validation section.

Next, a section describing improvements on the original model regarding its convergence characteristics. Lastly, a section describing an alternative way of improving the simulation methodology, by implementing an SMA simulator, is described.

3.1 EOA simulator architecture

Figure 3-1 summarizes the calculation process carried out by the simulator. Initially, the user inputs a block diagram and its respective process parameters into the GUI. Blocks and streams, collectively referred in Figure 3-1 as elements, supply equations to the simulation engine, which assembles the GSOE. The equations then facilitate convergence based on specific instructions.

This global system of equations is then passed on to a solver (MATLAB Trust-Region or NR, for instance), along with a vector of initial estimates, which proceeds to solve the system. Once the system is solved, the simulator produces a report containing the values of all process variables, as calculated by the simulator.

Initial estimates may either be directly supplied by the user or by the simulator itself, which defaults estimates to zero if not provided. This architecture allows for any variable to remain constant. Suppose it is desired that variable x , belonging to element 1, remain constant at a prespecified value of ten. All that must be done is to require that element 1 provide the engine with the equation $x - 10 = 0$.

The ordering process begins by constructing a bipartite graph corresponding to the GSOE (Fritzson, 2010). In this graph, two sets of vertices exist: equation vertices and variable vertices. An edge connects equation vertex i to variable vertex j if variable j takes part in equation i . As an example, suppose that the GSOE consists of the three equations shown in equation 3.1:

$$\begin{cases} f(x_1) = 0 \\ f(x_1, x_2, x_3) = 0 \\ f(x_2, x_3) = 0 \end{cases} \quad (3.1)$$

The bipartite graph corresponding to this system of equations is shown in Figure 3-2(a), where the squares represent equations and the circles represent variables.

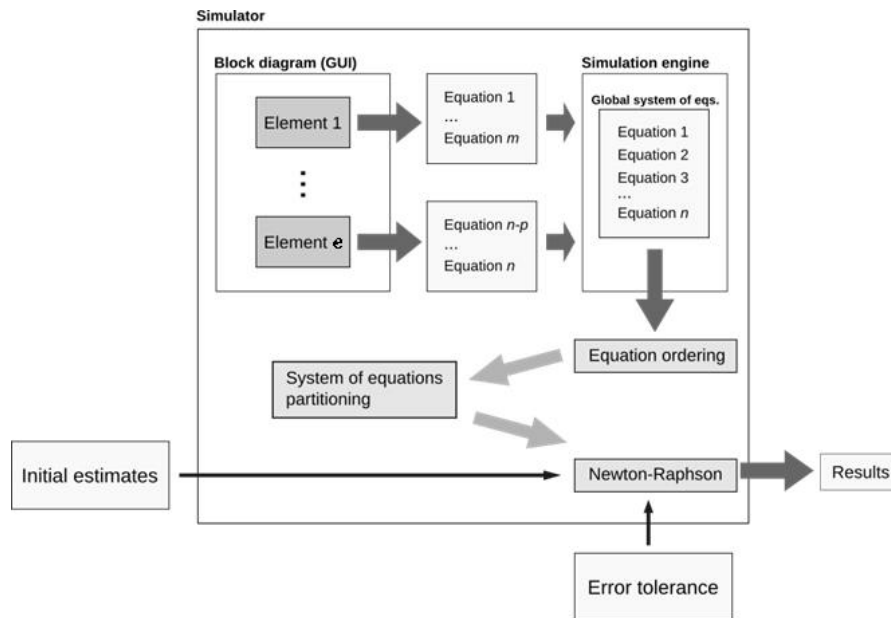


Figure 3-1: Steps taken by the EOA simulator during the calculation of an MEE process flowsheet.

Given a bipartite graph, a matching is defined as a set of edges such that no edges share a vertex. A matching is said to be maximal if no matching exists with a higher number of edges (Fritzson, 2010). In the current example, the three bold edges shown in Figure 3-2(b) form a matching, since none of these edges share a vertex. Notice that a matching cannot exist with a higher number of edges, as that would cause an equation to be shared between two edges. Therefore, the bold edges constitute a maximum bipartite matching of size three.

In the simulator, the maximum bipartite matching, M , for this graph is determined using the Ford-Fulkerson algorithm (Sedgewick and Wayne, 2011). The bipartite graph is then converted into a directed graph through the following process: for every edge e connecting equation vertex i to the variable vertex j , if e belongs to M , then replace it with a directed edge connecting i to j . If e is not in M , then replace it with a directed edge connecting j to i . The topological ordering of this directed graph gives the ordering of the equations (Fritzson, 2010). The result of applying this procedure to the current example is displayed in Figure 3-2(c).

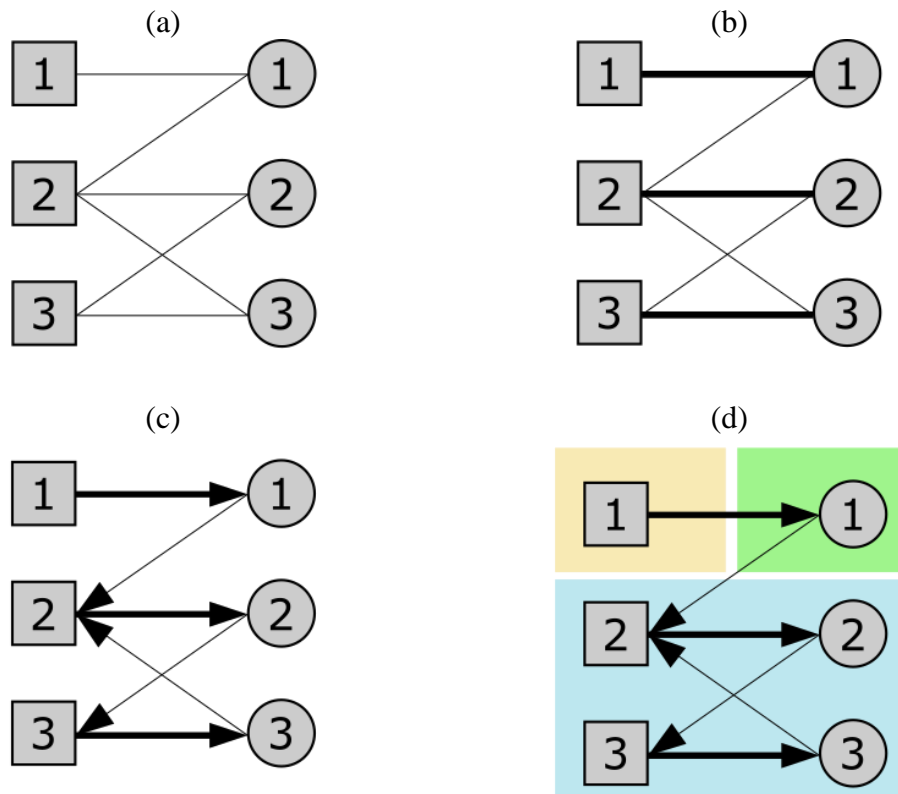


Figure 3-2: Equation ordering and partitioning procedure starting from the bipartite graph corresponding to the GSOE.

Once the order of the equations has been determined, the simulator determines the subsets of equations that need to be solved simultaneously. This step is referred to as *partitioning*. From a computational standpoint, partitioning is equivalent to finding the strongly connected components, or SCCs, of the ordered graph. In the simulator, this step is done with the well-known Kosaraju algorithm (Sedgewick and Wayne, 2011). The result of partitioning the current example is displayed in Figure 3-2(d). The ordered graph contains a total of three partitions, each of which is highlighted with a different background color. This partitioning step produces a complete calculation sequence for the GSOE. In the example provided, equation 1 is solved first, allowing variable 1 to be found. Then, equations 2 and 3 are solved together to find the values for variables 2 and 3.

The simulator solves each partition using the NR method. Initial estimates for the variables may either be supplied by the user or calculated by the simulator. In the latter case, the simulator is run using simplified models for each unit process to facilitate convergence, and the values upon which it converges are used as estimates.

3.2 SMA simulator architecture

Figure 3-3 summarizes the calculation process carried out by the SMA simulator. Initially, the user inputs a block diagram and its respective process parameters into the GUI. If the user wishes to supply initial estimates, it is also possible to do so. If no initial estimates are supplied, the simulator uses the default values.

The simulator then creates the calculation modules corresponding to each GUI element, bringing to the module all user input information necessary for making a calculation. The simulator also generates an information flow graph representing the dependencies of each module with respect to every other module, as shown in Figure 3-4. For example, an evaporator body requires data from its input vapor and black liquor streams and supplies data to the outlet vapor, condensate, and black liquor streams. Therefore, as shown in Figure 3-4, in the information flow graph the vertex corresponding to the evaporator will have incoming edges from its input streams and outgoing edges to its outlet streams.

The information flow graph is then processed to identify all its *circuits*. A circuit is a loop within the graph made up of a sequence of non-repeating vertices and edges. If an edge is removed from this graph, then at least one loop will have been removed from the graph, which is equivalent to tearing a stream in the flowsheet. Therefore, repeatedly removing edges from the set of circuits of a graph eventually leads to an acyclic graph, which corresponds to a flowsheet with no remaining untear recycle streams. By listing the set of all circuits in a graph, it is possible to select the smallest set of edges that, when removed, cause the graph not to have any loops.

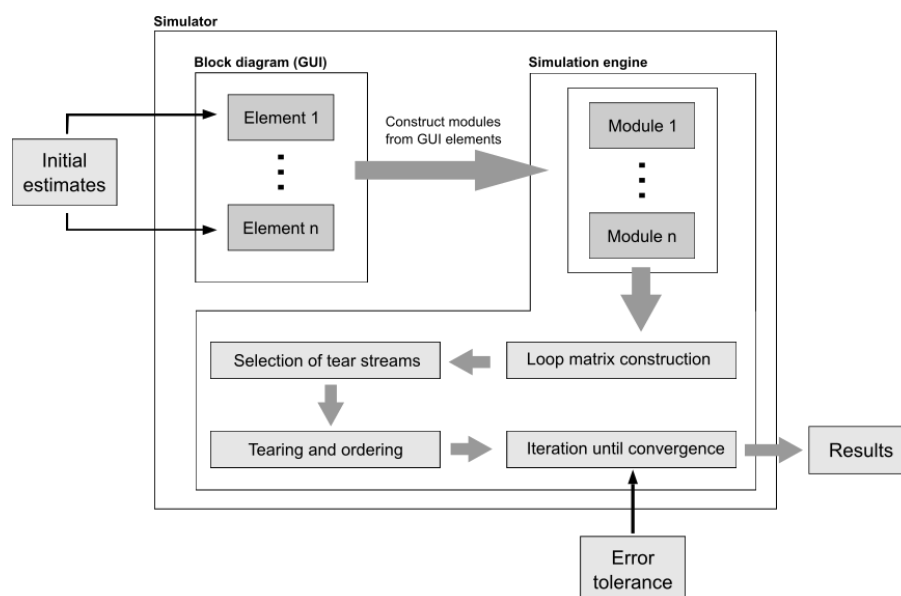


Figure 3-3: Steps taken by the SMA simulator during the calculation of an MEE process flowsheet.

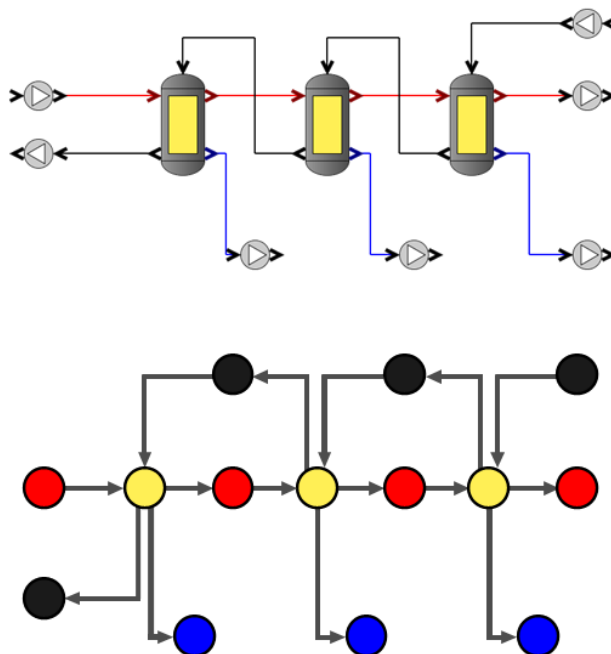


Figure 3-4: Information flow graph (below) corresponding to an MEE process flowsheet (above). Evaporators and streams are represented by circles. Evaporators are displayed in yellow, vapor streams in red, condensate streams in blue, and black liquor streams in black. The arrows represent calculation dependencies.

The set of all circuits was constructed by traversing the information flow graph using a depth-first search (DFS) (Sedgewick and Wayne, 2011).

Once the set was constructed, a *loop matrix*, \mathbf{L} , was constructed. In this matrix, each column corresponded to an edge and each row to a circuit. Element $L_{i,j}$ is equal to one if circuit i contains edge j , otherwise it is equal to zero. Notice that the sum of all elements under column j is equal to the number of circuits in which an edge participates. This gives rise to the following greedy heuristic for removing edges:

- Identify the edge that participates in the most circuits;
- Remove the edge from \mathbf{L} and all circuits that contained it;
- Repeat the steps above while circuits still remain in \mathbf{L} .

The edges that have been removed are each associated with a single stream in the flowsheet. These streams form a set of tearing streams.

Now that the information flow graph has been rendered acyclic, the calculation order can easily be determined by running a topological sort on it. At this point, the calculations may begin.

In every iteration, the simulator loops through each of the modules in the order determined by the topological sort and keeps a cache of all torn stream variables. If the maximum relative error among all torn steam variables over two consecutive iterations is smaller than a predetermined relative tolerance, usually on the order of 1%, then the simulator stops and is assumed to have converged. Otherwise, another iteration is executed.

The simulator modifies the calculated torn stream variable values after each iteration using Wegstein's method, which is quite common in commercial process simulators and can greatly improve the likelihood and rates of convergence (Smith, 2016).

3.3 Supported unit processes, blocks, and streams

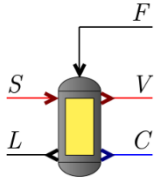
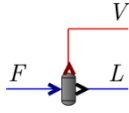
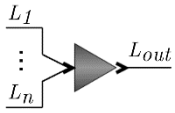
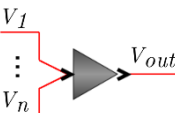
The unit processes currently supported by the simulator are as follows: evaporation, black liquor and condensate flashing, black liquor mixing and vapor and condensate mixing. The mass flows that take place between the unit processes are represented by streams that are divided into black liquor, vapor, and condensate streams.

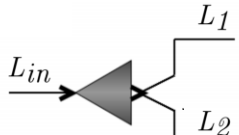
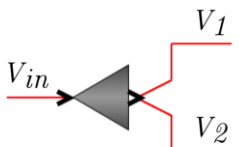
Table 3.1 lists the variables that describe each type of stream and Table 3.2 lists the currently supported process blocks and the equations corresponding to each of them. In these equations, variable subscripts denote the streams to which they correspond, except for subscript *sat*, which denotes saturation. Mass flows are indicated by \dot{m} , enthalpies by H , temperatures and pressures by T and P , respectively, the dissolved solids mass fraction by x_D , the total solids mass fraction by x_T , and the boiling point rise of black liquor by BPR . Black liquor streams are graphically depicted by black lines. Vapor and condensate streams are in turn depicted as red and blue lines, respectively.

Table 3.1: Stream types supported by the EOA and SMA simulators and the variables that describe them. The subscripts *D* and *T* denote dissolved and total solids fractions, respectively.

Stream type	Variables
Vapor	\dot{m}, T, P
Condensate	\dot{m}, T, P
Black liquor	\dot{m}, T, x_D, x_T

Table 3.2: Unit processes supported by the EOA and SMA simulators and the equations that describe them

Process block	Description	Equations
 <p>Evaporator</p>	<p>The black liquor stream, F, and the inlet vapor stream, S, enter the evaporator block. The outlet black liquor stream, L, the condensate stream, C, and the outlet vapor stream, V, exit the block. Evaporator blocks take as parameters the heat transfer coefficient, U, and the heat transfer area, A.</p>	$\begin{aligned} \dot{m}_S &= \dot{m}_C \\ \dot{m}_F &= \dot{m}_L + \dot{m}_V \\ \dot{m}_F x_{D,F} &= \dot{m}_L x_{D,L} \\ \dot{m}_F x_{T,F} &= \dot{m}_L x_{T,L} \\ P_S &= P_C \\ T_C &= T_{sat}(P_S) \\ T_V &= T_{sat}(P_V) + BPR(P_V, x_{D,L}) \\ T_V &= T_L \\ Q &= \dot{m}_S(H_S - H_C) \\ Q &= UA(T_S - T_L) \\ \dot{Q} + \dot{m}_F H_F &= \dot{m}_L H_L + \dot{m}_V H_V \end{aligned}$
 <p>Flash tank</p>	<p>The inlet black liquor or condensate stream, F, enters the flash block. The outlet vapor stream, V, and the outlet black liquor or condensate stream, L, exit the block. The flash tank pressure is determined by the outlet vapor stream pressure, P_V.</p>	$\begin{aligned} \dot{m}_F &= \dot{m}_L + \dot{m}_V \\ T_V &= T_L \\ P_V &= P_{sat}(T_V) \\ P_L &= P_{sat}(T_V) \\ \dot{m}_F x_{D,F} &= \dot{m}_L x_{D,L} \\ \dot{m}_F x_{T,F} &= \dot{m}_L x_{T,L} \end{aligned}$
 <p>Black liquor mixer</p>	<p>An arbitrary number of black liquor streams, L_i, enter the mixer block and a single combined black liquor stream, L_{out}, exits it.</p>	$\begin{aligned} \sum_i \dot{m}_i &= \dot{m}_{out} \\ \sum_i \dot{m}_i H_i &= \dot{m}_{out} H_{out} \\ \sum_i \dot{m}_i x_{D,i} &= \dot{m}_{out} x_{D,out} \\ \sum_i \dot{m}_i x_{T,i} &= \dot{m}_{out} x_{T,out} \end{aligned}$
 <p>Vapor mixer</p>	<p>An arbitrary number of vapor or condensate streams, V_i, enter the mixer block and a single combined vapor or condensate stream, V_{out}, exits it. In this work, the vapor mixer is assumed to cause a negligible pressure drop and that all pressures will be equal.</p>	$\begin{aligned} \sum_i \dot{m}_i &= \dot{m}_{out} \\ \sum_i \dot{m}_i H_i &= \dot{m}_{out} H_{out} \\ P_1 = P_2 = \dots = P_n &= P_{out} \end{aligned}$

 <p>Black liquor splitter</p>	<p>An inlet black liquor stream is split it into two outlet streams, whose mass flows are defined by a splitter ratio R. The outlet streams are assumed to have the same values of temperature and solids fractions as the inlet stream.</p>	$\begin{aligned} \dot{m}_1 &= R\dot{m}_{in} \\ \dot{m}_2 &= (1 - R)\dot{m}_{in} \\ T_1 &= T_2 = T_{in} \\ x_{D,1} &= x_{D,2} = x_{D,in} \\ x_{T,1} &= x_{T,2} = x_{T,in} \end{aligned}$
 <p>Vapor splitter</p>	<p>An inlet vapor stream is split it into two outlet streams, whose mass flows are defined by a splitter ratio R. The outlet streams are assumed to have the same values of temperature and pressure as the inlet stream.</p>	$\begin{aligned} \dot{m}_1 &= R\dot{m}_{in} \\ \dot{m}_2 &= (1 - R)\dot{m}_{in} \\ T_1 &= T_2 = T_{in} \\ P_1 &= P_2 = P_{in} \end{aligned}$

3.3.1 A simplified evaporator model

As will be discussed in later sections, solving the nonlinear equations shown in Table 3.2 with NR requires that reasonably good initial estimates be provided. For this reason, an alternative, simplified evaporator model was developed. Solving this model is far easier in terms of convergence, and the results obtained from it serve as good initial estimates for solving the system of equations corresponding to the original model. The simplified evaporator model is shown below:

$$\dot{m}_S = \dot{m}_C \quad (3.2)$$

$$\dot{m}_F = \dot{m}_L + \dot{m}_V \quad (3.3)$$

$$\dot{m}_F x_{D,F} = \dot{m}_L x_{D,L} \quad (3.4)$$

$$\dot{m}_F x_{T,F} = \dot{m}_L x_{T,L} \quad (3.5)$$

$$P_S = P_C \quad (3.6)$$

$$T_C = T_{sat}(P_S) \quad (3.7)$$

$$T_V = T_{sat}(P_V) + BPR(P_V, x_{D,L}) \quad (3.8)$$

$$T_V = T_L \quad (3.9)$$

$$\dot{Q} = 2200 \dot{m}_S \quad (3.10)$$

$$\dot{Q} = UA(T_S - T_L) \quad (3.11)$$

$$\dot{m}_S = \dot{m}_V \quad (3.12)$$

In the simplified model, the evaporator energy balance is replaced with $\dot{m}_S = \dot{m}_V$, the BPR is neglected, and the heat of steam condensation is approximated as $\dot{Q} = 2200 \dot{m}_S$. This procedure replaces the nonlinear equations representing energy balances, enthalpy, and BPR calculations with simple linear terms to generate a good enough approximate solution to serve as a starting point for solving for the full model.

The simplified model was created by setting up the EOA simulator to calculate a single evaporator body, and then changing the evaporator model equations until a good compromise between accuracy and general ease of convergence was found. To gauge the general ease of convergence of a proposed model, directed bipartite graphs corresponding to its GSOEs were generated, following the procedure described in Figure 3-2, and then plotted using a Python script that implemented a simple force-directed graph plotting algorithm (Frishman and Tal, 2009).

3.4 Physical properties

Energy balances require that the water steam enthalpies of black liquor are known. Water and steam enthalpies were calculated based on steam table correlations and implemented in C++, as described in the 2007 revised release of the International Association for the Properties of Water and Steam IAPWS Industrial Formulation of 1997 standard (Cooper *et al.*, 2007).

Black liquor enthalpies were calculated based on the correlation described by Zaman and Fricke (1996), which expresses the enthalpy of black liquor at 80°C, H_{80} , as shown in equation 3.13. In this equation, $H_{w,80}$ denotes the water enthalpy at 80°C, x_D is the black liquor dissolved solids fraction, and the constants b and c depend on the type of black liquor being considered. In this work, it was assumed that $b = 105.0$ kJ/kg.K and $c = 0.300$.

$$H_{80} = H_{w,80} + b \left[-1 + \exp\left(\frac{x_D}{c}\right) \right] \quad (3.13)$$

To account for black liquor enthalpies at other temperatures, H_{80} is corrected using the black liquor heat capacity correlation given by equation 3.14, where t stands for the temperature measured in °C (Tikka, 2008):

$$c_p = 4.216(1 - x_D) + \left[1.675 + \frac{3.31t}{1000.0}\right]x_D + \left[4.87 + \frac{20t}{1000.0}\right](1 - x_D)x_D^3 \quad (3.14)$$

The black liquor boiling point rise (BPR) also needs to be considered in evaporator calculations. BPR is accounted for using equations 3.15 and 3.16, where T_p is the boiling temperature of water at pressure P (Tikka, 2008):

$$BPR(P, x_D) = BPR_{\text{atm}}(x_D) \left[1 + \frac{0.6(T_p - 373.16)}{100}\right] \quad (3.15)$$

$$BPR_{\text{atm}}(x_D) = 6.173x_D - 7.48x_D^{1.5} + 32.747x_D^2 \quad (3.16)$$

3.5 Base scenarios

Two MEE scenarios adapted from the literature were used to a) test and validate the results produced by the model and to b) test the evaporator systems' topological optimization methodology. The first scenario, shown in Figure 3-5, is a simple three-effect system with intermediate flashing, adapted from (Tikka, 2008). This scenario will be referred to as S_1 .

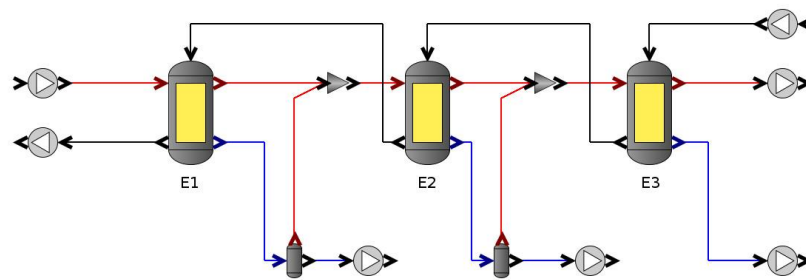


Figure 3-5: Simple three-effect MEE system (S_1), adapted from (Tikka, 2008).

Due to its simplicity, this scenario was useful for quickly testing whether the mathematical modeling yielded reasonable results and whether the proposed methodology would function as expected as well as for finding optimal ranges for the DE parameters. The second, more realistic scenario, referred to as S_2 , is shown in Figure 3-6. This system is a six-effect MEE plant, composed of seven evaporators, with intermediate condensate flashing as well as black liquor flashing.

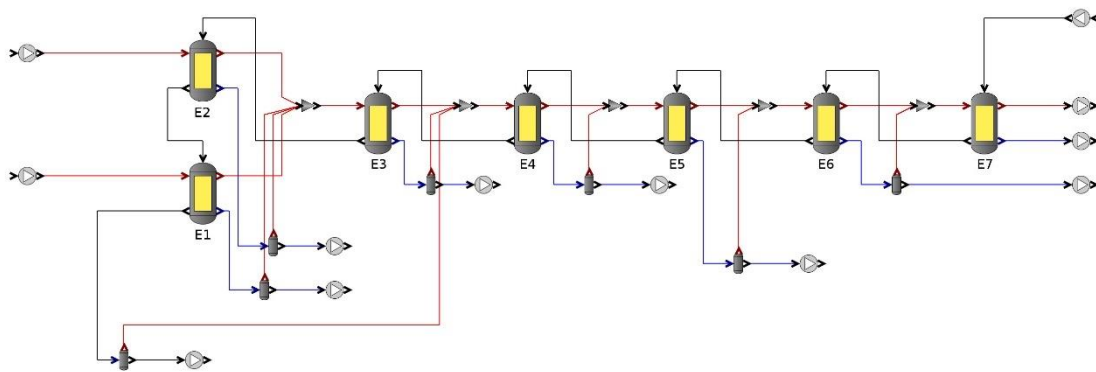


Figure 3-6: Realistic six-effect MEE system (S_2), adapted from (Saturnino, 2012).

3.6 Model validation

It is necessary to first verify whether the model would yield reasonable values compared to the reference data. To do that, both systems S_1 and S_2 were simulated using the EOA simulator and input data taken from the literature, and the values produced by the simulator were compared to those found in the references. Table 3.3 displays the input data used for validating S_1 , which was taken from a sample MEE calculation scenario (Tikka, 2008).

Table 3.3: Input validation values for the three-effect system, S_1 (reference values taken from (Tikka, 2008))

Variable	Value	Units
Live steam temperature	120	°C
Black liquor inlet mass flow	50	kg/s
Black liquor inlet temperature	70	°C
Black liquor inlet dissolved solids	20	%
Vapor temperature from Effect 3	60	°C
Heat transfer coefficient of Effect 1 (U1)	1.2	kW/m ² K
Heat transfer coefficient of Effect 2 (U2)	1.6	kW/m ² K
Heat transfer coefficient of Effect 2 (U3)	2.0	kW/m ² K
Outlet black liquor dissolved solids	50	%

Table 4 displays the input data used for validating S_2 . These values are more realistic and were taken from (Saturnino, 2012).

Table 3.4: Input validation values for the six-effect system, S_2 (reference values derived from (Saturnino, 2012))

Variable	Value	Units
Live steam temperature to Effect 1	140	°C
Live steam temperature to Effect 2	147	°C
Vapor temperature from Effect 7	52	°C
Black liquor inlet mass flow	15.6	kg/s
Black liquor inlet temperature	64.7	°C
Black liquor inlet dissolved solids	11.8	%
Black liquor outlet dissolved solids	31	%
Heat transfer coefficient of Effect 1 (U1)	0.296	kW/m ² K
Heat transfer coefficient of Effect 2 (U2)	0.4303	kW/m ² K
Heat transfer coefficient of Effect 3 (U3)	0.2584	kW/m ² K
Heat transfer coefficient of Effect 4 (U4)	0.6955	kW/m ² K
Heat transfer coefficient of Effect 5 (U5)	0.839	kW/m ² K
Heat transfer coefficient of Effect 6 (U6)	0.9698	kW/m ² K
Heat transfer coefficient of Effect 7 (U7)	1.224	kW/m ² K

Once the simulator was capable of outputting values in agreement with the reference values, it was deemed suitable for optimization.

3.7 Expanding the base scenarios using the EOA simulator

S_1 and S_2 were considered to undergo a 15% increase in the black liquor feed rate over the values shown in tables Table 3.3 and Table 3.4. To maintain the same final dissolved solids concentration, new evaporator bodies are added to these systems. The objective of

this optimization scenario is to find the best arrangement for the new evaporator(s) and its(their) heat transfer area(s). Although this methodology allows for an infinite number of evaporator body arrangements to be considered, the problem was here constrained to only encode the possibilities of adding an evaporator in series and/or in parallel to the existing systems.

To encode these possibilities, the new flowsheets shown in figures Figure 3-7 and Figure 3-8 are drawn. In this diagram, two possible new evaporators, E_{par} and E_{ser} , having heat transfer areas equal to A_{par} and A_{ser} and are added to the original systems along with new mixers and splitters. By changing the splitter fractions of the splitters feeding black liquor and vapor streams to the new evaporators, an infinite number of arrangements can be encoded.

This diagram has the property of encoding multiple tentative topological arrangements by means of varying the splitter fractions, making it useful for optimization. Diagrams with such a property have been described in the literature as *superstructures*, a nomenclature that is also adopted in this study (Biegler, Grossmann and Westerberg, 1997).

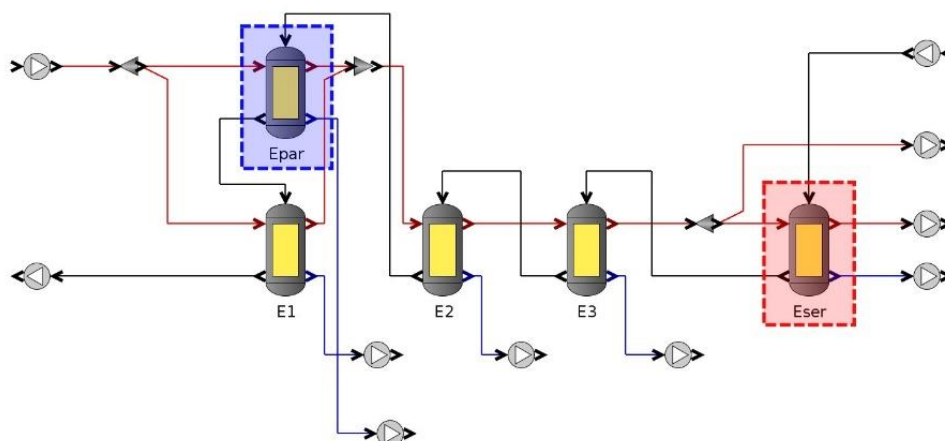


Figure 3-7: Superstructure encoding two typical possibilities (parallel/series) for expanding the three-effect train (S_1).

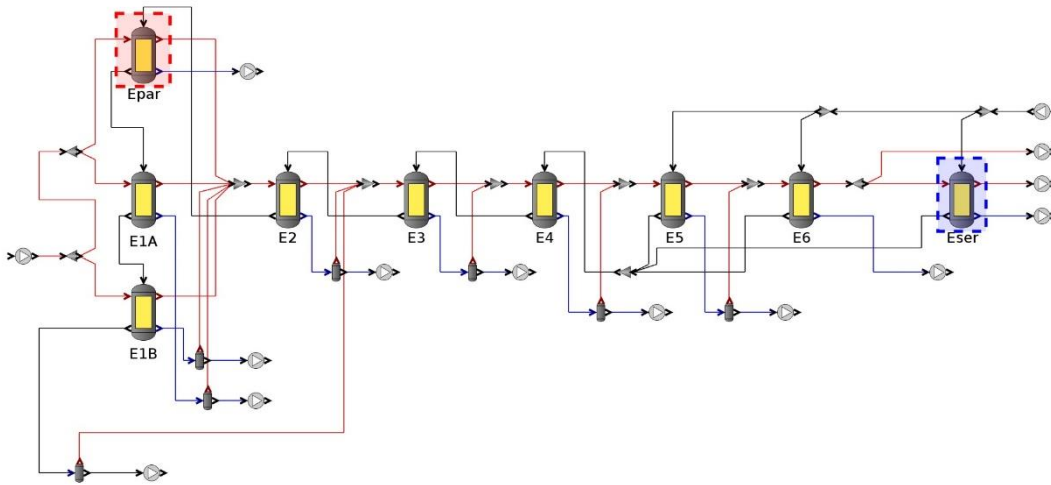


Figure 3-8: Superstructure encoding two typical possibilities (parallel/series) for expanding the six-effect train (S_2).

To evaluate the cost of a proposed arrangement, a cost model must be adopted. In this study, the cost of a proposed evaporator arrangement with total heat transfer area A is given via equation 3.17, where the constant coefficients come from the professional experience of the author and his collaborators. This equation gives cost c in USD. The optimization goal is to select the arrangement that yielded the lowest value for c . It should be noted that the aim of this dissertation is not to give accurate estimates of the costs involved, as those may vary significantly in different parts of the world, but to present a methodology for optimizing evaporator systems that consider all feasible topological arrangements.

$$c = 30\,000 + 1\,000A^{0.9} \quad (3.17)$$

The evaporator plants in this study are each modeled via a system of nonlinear equations representing their mass and energy balances, which, when solved, yield a steady-state solution for the system. Determining the optimal arrangement for the new evaporator corresponds to solving an optimization problem, whose choice variables encode the different arrangement possibilities and whose objective function quantifies the cost of adding the new heat transfer surface. In this study, the optimization itself is carried out by means of DE.

This metaheuristic was chosen to be the optimizer because it is widely used and because of its success in solving a variety of difficult multi-modal engineering optimization

problems combining continuous and discrete variables (Afanasyeva *et al.*, 2013; Saari *et al.*, 2014, 2019)

In the following section, we describe how the EOA simulator was used along with DE to perform the desired topological optimization.

3.7.1 Calculations

To ensure reliable convergence of the actual model, a simplified system is first used to generate a starting point for solving the full model. The equations remain essentially unchanged for all blocks, except the evaporator, which had its energy balance equation simplified. In this stage of simulator development, all the code was written in MATLAB and the equation partitioning and ordering subroutines had not yet been implemented. In other words, all the equations composing the GSOE were solved simultaneously. For this reason, solving the simplified system was particularly useful, as good initial estimates greatly facilitate the convergence of such large systems of equations.

In the simplified model, the evaporator energy balance is replaced with $\dot{m}_S = \dot{m}_V$, the BPR is neglected, and the heat of steam condensation is approximated as $\dot{Q} = 2200 \dot{m}_S$. More details can be found in section 3.3.1. This procedure replaces the nonlinear equations representing energy balances, enthalpy, and BPR calculations with simple linear terms to generate a good enough approximate solution to serve as a starting point for solving for the full model.

As stated previously, the goal of the optimization problems was to find the least costly arrangement for the new evaporator body, or evaporator bodies, as well as the heat transfer areas capable of meeting the same outlet liquor dry solids concentration as before.

For each combination of splitter fractions and heat transfer areas, the system of equations corresponding to the superstructure under study was solved to find the final black liquor concentration rate. The systems were solved via MATLAB's implementation of the trust-region method, whose convergence depends on the quality of the initial estimate. Due to the difficulty of finding an initial estimate that guarantees convergence, it proved necessary to include all the model variables in the optimization problem.

The calculation proceeded as follows (see Figure 3-9):

1. For each generation, DE generates a vector containing all variables describing the system, including both the optimization variables (splitter fractions and heat transfer areas) and non-optimization variables related to solving the system (mass flows, pressures, temperatures, and solid fractions);
2. The optimization variables are given to the simulator as fixed parameters; the vector with all variables is used as an initial estimate. The simulator is then run

with the simplified model. This extra step was important, for it substantially increased the likelihood of convergence. If no solution was found, the objective function would return a constant of 10^{15} ;

3. The values found for the variables based on solving the simplified model are used as initial estimates for the complete model. If a solution is found, equation 3.17 is evaluated to obtain the cost, and this value is returned to DE; otherwise, the constant 10^{15} was returned. If the trust-region algorithm converges but with negative (thus, physically impossible) values for some of the variables, the objective function value is set at $10^{12} \times n_{\text{neg}}$, where n_{neg} is the number of negative values. If the outlet black liquor concentration is smaller than required, the cost function is penalized by $10^{12}(x_D^{\text{spec}} - x_D^{\text{out}})$, where x_D^{spec} is the specified outlet-dissolved solids concentration and x_D^{out} is the actual solids concentration.

The goal of the penalty scheme was to ensure that a candidate that fails to converge in the solver should lose out to any candidate that does converge; among candidates where the solver converges, one that violates constraints should always lose out to any legal candidate, no matter how poor otherwise, whereas between candidates that violate constraints, the one that violates fewer constraints should win.

The constants 10^{12} and 10^{15} were chosen so that they would penalize the objective function with a relatively high value if the solver did not converge and with a still relatively high value, although lower, if it converged but with the constraints having been violated. Notice that a 10^{12} term is added to the total penalty for each violated constraint. The equations were solved using MATLAB's implementation of the trust-region algorithm with numerically evaluated derivatives.

The algorithm was assumed to have converged when either the Euclidean distance between the points of two successive iterations was less than 10^{-12} or when the absolute difference between two successive objective function evaluations was less than 10^{-12} . To increase the probability of the points generated via DE converging at a feasible solution, upper and lower bounds were calculated for each problem based on their input parameters.

3.7.2 Optimization parameters

S₁ was used to assess the validity and practicality of the proposed methodology, as it is a relatively small system. The lower and upper bounds assigned to each optimization variable are listed in Table 3.5. For this problem, the number of choice variables, D , is equal to 87.

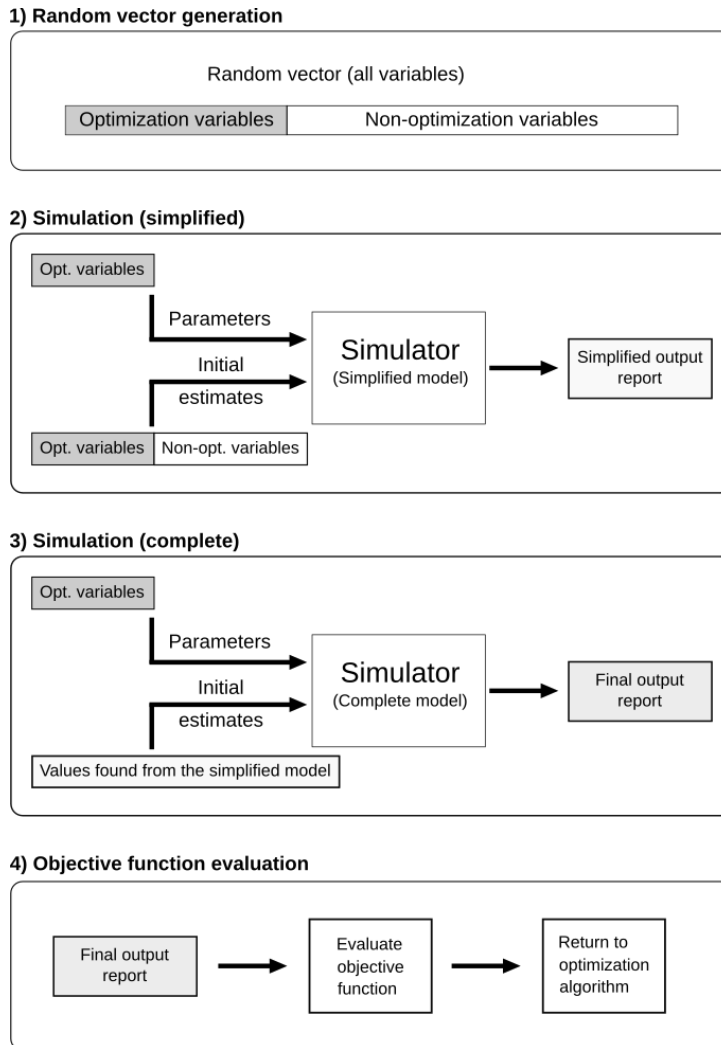


Figure 3-9: Steps involved in evaluating the objective function.

The problem was solved with DE for multiple combinations of Np and F , with CR fixed at 0.9. The goal was to identify the set of values for these parameters that allowed the problem to be solved both correctly and as efficiently as possible. For each combination of points, five trials were conducted.

Table 3.6 displays the DE parameters used and shows their corresponding ranges and the number of sampled points within that range. For example, Np varied from 20 to 100 over a sample of five points, meaning that Np could assume values of 20, 40, 60, 80, or 100. The algorithm would terminate when the number of function evaluations (NFE) exceeded 5000. In total, $5 \times 4 \times 5 = 100$ runs were conducted.

Table 3.5: Lower and upper bounds for S_1

Variable	Lower bound	Upper bound	Units
Liquid stream temperatures	40	120	°C
Vapor stream temperatures	40	120	°C
Vapor stream pressures	7.38	198.73	kPa
Liquid stream flows	0	50	kg/s
Vapor stream flows	0	50	kg/s
Exchanged heat	0	73000	kW
Heat transfer areas	400	4000	m ²
Dissolved dry solids	0.2	0.5	–
Total dry solids	0.2	0.5	–
Splitter fractions	0	1	–

Table 3.6: DE parameters corresponding to S_1

Parameter	Range	Sampled points in range	Stopping criterion
NP	[20, 100]	5	
F	[0.4, 1.0]	4	NFE = 5000
CR	0.9	1	

S_2 is a larger scenario, one used to assess whether the proposed methodology could optimize realistically sized systems. For this system, $D = 218$. Table 3.7 shows the upper and lower bounds that were used. As before, S_2 was solved with DE for multiple combinations of NP and F , with CR fixed at 0.9. For each combination, five trials were conducted. The runs were interrupted when NFE exceeded 75000. The exact parameter ranges and sample sizes can be found in Table 3.8.

A total of $3 \times 2 \times 5 = 30$ runs were executed. The number of sample points chosen was smaller than in S_1 due to its greater level of complexity and increased required computational time.

Table 3.7: Lower and upper bounds for S_2

Variable	Lower bound	Upper bound	Units
Liquid stream temperatures	40	120	°C
Vapor stream temperatures	40	120	°C
Vapor stream pressures	7.38	198.73	kPa
Liquid stream flows	0	48.14	kg/s
Vapor stream flows	0	5.18	kg/s
Exchanged heat	6000	47000	kW
Heat transfer areas	300	3000	m ²
Dissolved dry solids	0.1393	0.7	–
Total dry solids	0.1393	0.7	–
Splitter fractions	0	1	–

Table 3.8: DE parameters corresponding to S_2

Parameter	Range	Sampled points in range	Stopping criterion
Np	[64, 256]	3	
F	[0.5, 0.8]	2	NFE = 75000
CR	0.9	1	

3.8 Improving the convergence characteristics of the EOA simulator

The evaporator optimization methodology described in the last section may experience numerical difficulties during its execution when evaporators are operating close to the point where boiling begins. This is the case because the set of equations that model the evaporators, shown in Table 3.2, assume that a liquid-vapor equilibrium has been established. As the optimization calculations are executed, it may be the case that in a given iteration, some of the evaporator bodies do not transfer enough heat to the black liquor to raise its temperature to the boiling point. In this iteration, therefore, the evaporation assumption will not hold, which may lead the simulator to either diverge or converge at an incorrect solution.

To alleviate this problem and attempt to broaden the convergence region of the model, a modification was proposed for the original evaporator model. The new equations are shown below:

$$\dot{m}_S = \dot{m}_C \quad (3.18)$$

$$\dot{m}_F = \dot{m}_L + \dot{m}_V \quad (3.19)$$

$$\dot{m}_F x_{D,F} = \dot{m}_L x_{D,L} \quad (3.20)$$

$$\dot{m}_F x_{T,F} = \dot{m}_L x_{T,L} \quad (3.21)$$

$$T_C = T_{sat}(P_S) \quad (3.22)$$

$$T_{bp} = T_{sat}(P_V) + BPR \quad (3.23)$$

$$BPR = BPR(P_V, x_{D,L}) \quad (3.24)$$

$$T_V = T_L \quad (3.25)$$

$$\dot{Q} = \dot{m}_S(H_S - H_C) \quad (3.26)$$

$$\dot{Q} = UA(T_S - T_L) \quad (3.27)$$

$$\dot{Q} + \dot{m}_F H_F = \dot{m}_L H_L + \dot{m}_V H_V \quad (3.28)$$

$$\dot{Q}_1 = \dot{m}_F (H_F^{bp} - H_F) \quad (3.29)$$

$$\begin{aligned} &\text{If } \dot{Q} < \dot{Q}_1 \\ &\quad \dot{m}_V = 0 \\ &\text{Else} \\ &\quad T_V = T_{bp} \end{aligned} \quad (3.30)$$

Notice that three new variables were introduced: \dot{Q}_1 , BPR , and T_{bp} . \dot{Q}_1 denote the necessary power to raise the black liquor temperature from its feed temperature to its boiling point, where the liquor enthalpy is equal to H_F^{bp} . BPR denotes the boiling point rise. Even though it had already been considered in the original model, it has been given its own separate variable for the sake of convenience.

The form taken by equation 3.30 depends on the value of \dot{Q}_1 . In the original model, the equality between the outlet liquid temperature and the liquor boiling point (the equilibrium condition) was always enforced. This, however, is not necessarily the case here. If the supplied heat, \dot{Q} , is such that $\dot{Q} < \dot{Q}_1$, then not enough heat is available to cause the liquor temperature to rise to its boiling point. In this case, no vapor is produced and all \dot{Q} is spent increasing the liquor temperature. Under this condition, the equilibrium condition equation is replaced with $\dot{m}_V = 0$.

3.8.1 Test cases

To assess the quality of the new model, three test cases were considered: a single evaporator body, a simple three-effect MEE train, and a more realistic seven-effect MEE train. The latter two systems were loosely adapted from the base scenarios S_1 and S_2 described in section 3.5. The intermediate flashing, however, was omitted to isolate the evaporator model's behavior as much as possible.

The single evaporator scenario was assumed to have a heat transfer coefficient of $U = 1.2$ kW/m²K and a heat transfer area of 1 000 m². Its black liquor inlet and outlet properties were equal to those of the three-effect system, shown in Table 3.9.

Figure 3-10 displays the flowsheet of the simple three-effect MEE train being considered and Table 3.9 displays the input variable values fed to it during the tests. The values for the live steam temperature, black liquor inlet mass flow, inlet total, and dissolved solids, as well as the heat transfer area, were also used for the single evaporator body tests.

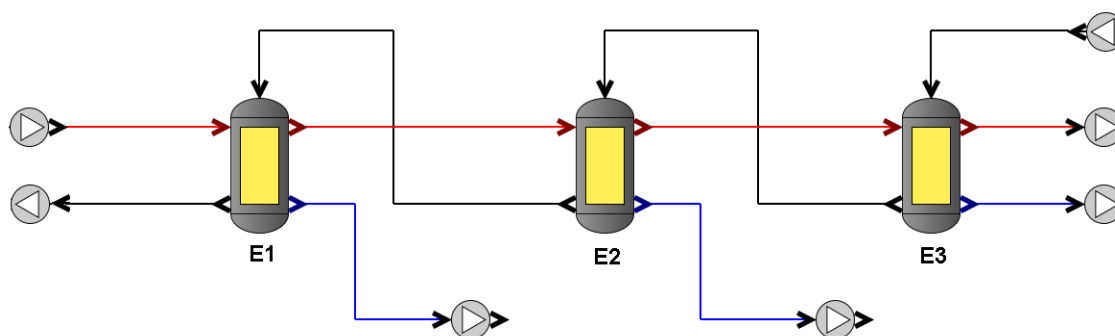


Figure 3-10: Simple three-effect MEE train adapted from S_1 .

Table 3.9: Input values for the simple three-effect MEE train adapted from S_1

Variable	Value	Units
Live steam temperature	120	°C
Black liquor inlet mass flow	50	kg/s
Black liquor inlet temperature	70	°C
Black liquor inlet dissolved solids	20	%
Black liquor inlet total solids	20	%
Vapor temperature from Effect 3	60	°C
Heat transfer coefficient of Effect 1 (U_1)	1.2	kW/m ² K
Heat transfer coefficient of Effect 2 (U_2)	1.6	kW/m ² K
Heat transfer coefficient of Effect 2 (U_3)	2.0	kW/m ² K
Outlet black liquor dissolved solids	50	%
Heat transfer area (all effects)	1 000	m ²

Figure 3-10 displays the flowsheet of the realistic seven-effect MEE train being considered and Table 3.9 displays the input variable values fed to it during the tests.

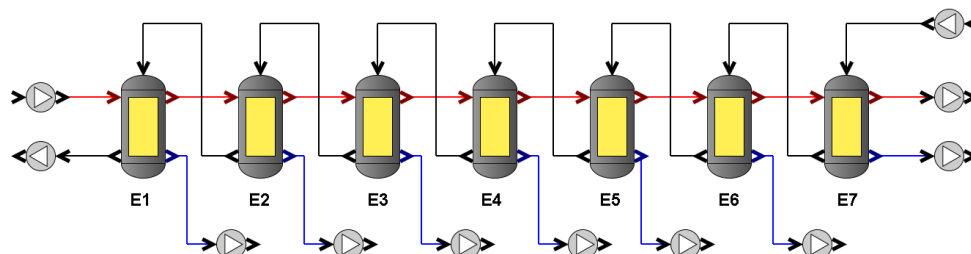


Figure 3-11: Realistic seven-effect MEE train loosely adapted from S_2 .

Table 3.10: Input values for the realistic seven-effect MEE train loosely adapted from S_2

Variable	Value	Units
Live steam temperature to Effect 1	120	$^{\circ}\text{C}$
Live steam mass flow	2.0	Kg/s
Black liquor inlet mass flow	15.6	kg/s
Black liquor inlet temperature	64.7	$^{\circ}\text{C}$
Black liquor inlet dissolved solids	11.8	%
Black liquor inlet total solids	11.8	%
Heat transfer coefficient of Effect 1 (U1)	0.296	$\text{kW/m}^2\text{K}$
Heat transfer coefficient of Effect 2 (U2)	0.4303	$\text{kW/m}^2\text{K}$
Heat transfer coefficient of Effect 3 (U3)	0.2584	$\text{kW/m}^2\text{K}$
Heat transfer coefficient of Effect 4 (U4)	0.6955	$\text{kW/m}^2\text{K}$
Heat transfer coefficient of Effect 5 (U5)	0.839	$\text{kW/m}^2\text{K}$
Heat transfer coefficient of Effect 6 (U6)	0.9698	$\text{kW/m}^2\text{K}$
Heat transfer coefficient of Effect 7 (U7)	1.224	$\text{kW/m}^2\text{K}$
Heat transfer area (all effects)	1000	m^2

3.8.2 Convergence rate assessment

To assess how well the new model behaved, several simulations were executed for the single evaporator and for the three-effect MEE train using the new model for different combinations of the live steam mass flow and heat transfer area. These will be referred to as *test variables*. The test variable ranges and number of tested values for both systems are shown in tables Table 3.11 and Table 3.12.

Table 3.11: Test variables range for the single evaporator system

Variable	Range	Number of points
Live steam mass flow (kg/s)	[0 – 20]	100
Outlet vapor pressure (kPa)	[50 – 85]	5

Table 3.12: Test variables range for the three-effect MEE system

Variable	Range	Number of points
Live steam mass flow (kg/s)	[0 – 20]	20
Heat transfer area (m ²)	[1000 – 2000]	5

Unlike what was done with the original model, a simplified model was not used to generate initial estimates for the variables. Instead, random initial estimates were generated for each combination of test variables and the corresponding GSOE was solved for a maximum of $N_{\text{trials}} = 20\,000$ times, or until convergence. The initial estimates were uniformly sampled from the ranges shown in Table 3.13. This was done to minimize the possibility of divergence due to poor initial estimates. The seven-effect model was also simulated for a single typical scenario, namely the one shown in Table 3.10, to check the validity of its output variables.

The live steam mass flow and heat transfer area were chosen as test variables because they determine, to a great extent, the amount of heat needed for evaporation to occur. Since the new model was constructed to allow for more evaporative conditions to be simulated, experimenting with different values for these variables should give a good idea of how well the new model performs.

Table 3.13: Lower and upper bounds for the uniformly sampled initial estimates

Variable	Lower bound	Upper bound
Mass flow (kg/s)	0	20
Temperature (°C)	70	120
Pressure (kPa)	50	200
Heat load (kW)	0	10000
Boiling point rise (°C)	0	10
Dissolved solids fraction (-)	0.2	0.8
Total solids fraction (-)	0.2	0.8
Heat transfer area (m ²)	0	2000

3.9 Convergence characteristics of the SMA simulator

Another way to alleviate the difficulties caused by the boiling/non-boiling transition in evaporators is to implement the same original model described in Table 3.2 in an SMA

simulator. One of the advantages of this approach is that, since each module is calculated in isolation in this type of simulator, the problematic calculation cases can be taken care of within the evaporator module, hindering it from interfering with other calculations. From a practical standpoint, this also makes errors easier to diagnose and correct, since they can be traced back to each individual module as opposed to a GSOE.

The evaporator model was the same described by (Vianna Neto, Saari, *et al.*, 2020). The proposed iterative calculation scheme was obtained by assuming that the inlet vapor and liquor variables were known and that the outlet liquor, vapor, and condensate variables were unknown. Table 3.14 shows all the known and unknown parameters corresponding to all evaporator streams and to the evaporator body itself. The labels F , S , L , V , and C , as before, correspond to liquor feed, inlet vapor, outlet liquor, outlet vapor, and condensate, respectively.

Table 3.14: Known and unknown variables when calculating an evaporator in the SMA simulator

Variable	Evaporator	F	S	L	V	C
U	Known	-	-	-	-	-
A	Known	-	-	-	-	-
\dot{Q}	Unknown	-	-	-	-	-
\dot{m}	-	Known	Known	Unknown	Unknown	Unknown
x_D	-	Known	-	Unknown	-	-
x_T	-	Known	-	Unknown	-	-
P	-	-	Known	-	Unknown	Unknown
T	-	Known	Known	Unknown	Unknown	Unknown

As mentioned before, it is quite important to order and partition the system of equations to ensure convergence. For this reason, the same procedure for ordering and partitioning equations used for the EOA simulator was also used to determine the calculation sequence for the evaporator module.

3.9.1 Test scenarios

MEE systems ranging from 3 to 7 evaporator bodies were constructed, while maintaining the same counter-current structure shown in Figure 3-12.

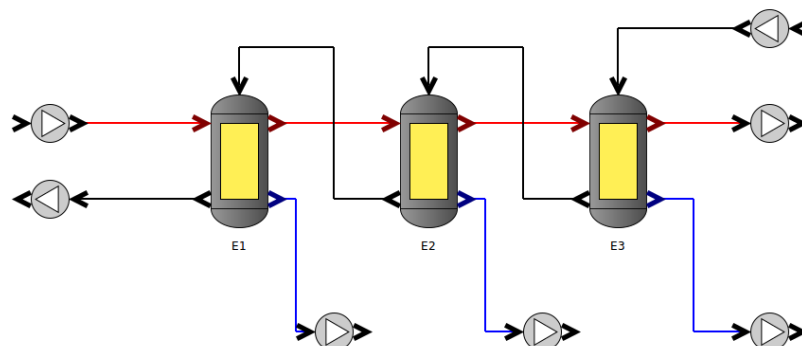


Figure 3-12: Base three-effect MEE system used for building similar larger systems.

The systems were initially simulated for three live steam mass flow values: 0, 2.5, and 5.0 kg/s. This first step was meant to assess how well the simulator could calculate scenarios where evaporation would not necessarily occur due to a low supply of steam. The number of iterations needed for convergence during each test was recorded. Table 3.15 lists the input values used for all tested scenarios.

Table 3.15: Input values for the generated MEE systems being used to test the SMA simulator

Variable	Value(s)	Units
Live steam temperature	120	°C
Live steam mass flow	0.0, 2.5 and 5.0	kg/s
Black liquor inlet mass flow	50	kg/s
Black liquor inlet temperature	70	°C
Black liquor inlet dissolved solids	20	%
Vapor temperature from Effect 3	60	°C
Heat transfer coefficient of all effects (U)	1.2	kW/m ² K
Heat transfer area of all effects (A)	1040	m ²

Each system was then simulated 100 times, with a fixed live steam mass flow of 5.0 kg/s, to measure the computational time required for the simulation to finish. This result is of great practical importance because the convergence time directly affects how practical it will be in optimization studies. The computer in which all the simulations were executed was equipped with a 2.7 GHz Intel® Core™ i7 and 4GB RAM and was run on Ubuntu 16.04. Convergence was assumed to be reached when the relative change in all variables in every torn stream was lower than 1%. The initial estimates used for the stream variables were values deemed as typical, and are shown in Table 3.16.

Table 3.16: Initial values for each variable used for the SMA simulator convergence tests.

Variable	Value(s)	Units
Vapor stream mass flows	1	kg/s
Vapor stream temperatures	100	°C
Vapor stream pressures	200	kPa
Black liquor stream mass flows	1	kg/s
Black liquor stream temperatures	100	°C
Black liquor stream dissolved solids	20	%
Black liquor stream total solids	20	%

4 Results and discussion

In the next two sections, the results corresponding to the calculation procedure and modeling and validation are presented. The results indicate that the model results display good agreement with the values found in the literature.

Next, the topological optimization results using the EOA simulator are given. The results prove that the research hypothesis is true, as the proposed methodology successfully optimized both proposed multiple-effect evaporator systems.

Following this section, the results corresponding to the proposed modification of the original model are given. They indicate that the modified model is capable of capturing scenarios where no evaporation takes place. They also suggest that the modified model suffers from convergence problems for large systems.

The last section presents the results obtained for the SMA simulator. The new simulator was shown to converge very well for evaporator systems ranging from 3-7 effects even when no evaporation takes place.

4.1 Simplified model

Figure 4-1 and Figure 4-2 display the plotted, GSOE-oriented bipartite graphs produced by calculating a single evaporator with the complete model and with the simplified model, respectively.

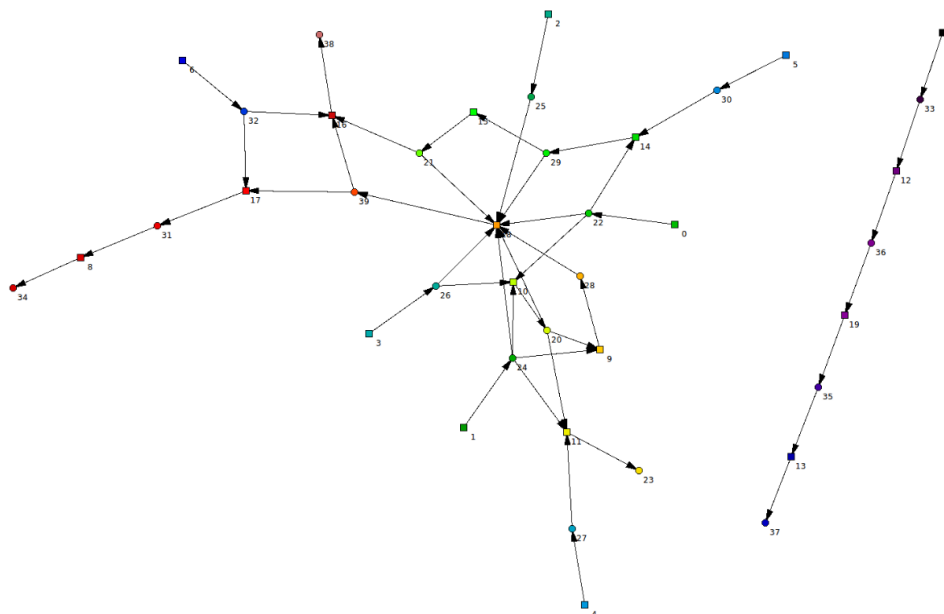


Figure 4-1: GSOE-oriented bipartite graph corresponding to a single evaporator using the complete evaporator model.

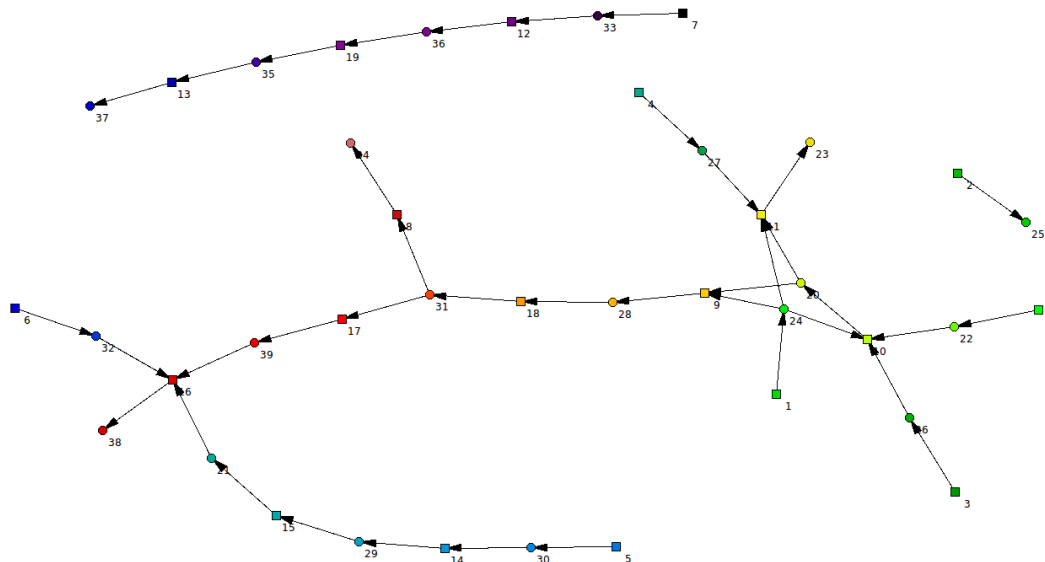


Figure 4-2: GSOE-oriented bipartite graph corresponding to a single evaporator using the simplified evaporator model.

In these figures, the square boxes correspond to equations and the circles correspond to variables following the same convention adopted in Figure 3-1. Figure 4-1 shows that the GSOE produces a graph containing two separate subsystems. The rightmost, somewhat linear chain of equations and variables corresponds to the relatively straightforward sequential pre-processing of input variables, such as calculating the live steam pressure based on its temperature and then equating it with the condensate pressure. The leftmost subsystem corresponds to the bulk of the calculations, where most mass and energy balances are found. Note that the graph's structure is quite intertwined due to the multiple interrelations that exist between variables and equations. From a practical standpoint, this means that in the partitioning stage, the EOA simulator will have to solve a relatively large part of these variables and equations together, thus making it that much more reliant on good initial estimates.

When contrasting Figure 4-1 with Figure 4-2, it is immediately apparent that the graph's structure is much more linear and less intertwined. In fact, this oriented graph has no loops, which allows each of its variables to be found sequentially. This structure sharply increases the likelihood of convergence for the simplified model, which makes it suitable for reliably generating initial estimates.

4.2 Evaporator model validation

Table 4.1 displays some of the key output variables calculated for the three-effect system as well as their reference values, taken from the original reference. Note that there is a strong agreement between the calculated and reference values. Nonetheless, the simulator underestimated the heat transfer area and the black liquor outlet temperature as compared to the reference values. This discrepancy is justified by the fact that the black liquor enthalpies in this work were calculated from different correlations than those of the original reference. All other calculated variables, however, agree with their corresponding reference values within a tolerance of under 7%.

Table 4.1: Comparison of calculated values and reference values for the three-effect system (derived from (Vianna Neto, Cardoso, Vakkilainen, *et al.*, 2020))

Variable	Calculated value	Reference value	Units	Relative error
Heat transfer areas (all effects)	810	1 040	m ²	22.12%
Vapor temperature from Effect 1	93.7	91.6	°C	2.29%
Vapor temperature from Effect 2	74.2	73.3	°C	1.23%
Vapor temperature from Effect 3	60	60	°C	0.00%
Black liquor dissolved solids from Effect 1	50	50	%	0.00%
Black liquor dissolved solids from Effect 2	33.3	33	%	0.91%
Black liquor dissolved solids from Effect 3	25.2	25	%	0.80%
Outlet black liquor temperature	93.7	99.8	°C	6.11%
Live steam mass flow	11.6	11.3	kg/s	2.65%

Table 4.2 displays some of the key output variables calculated for the six-effect system as well as their reference values, taken from the original reference. As before, there is a strong agreement between the calculated and reference values, and any discrepancies are likely due to the different correlations used. Note that the heat transfer areas are not shown in Table 4.2, as they were not reported in the original publication.

Table 4.2: Comparison of calculated values and reference values for the six-effect system (derived from (Vianna Neto, Cardoso, Vakkilainen, *et al.*, 2020))

Variable	Calculated value	Reference value	Units	Relative error
Vapor temperature from Effect 1	129	106.3	°C	21.35%
Vapor temperature from Effect 2	128.5	126.8	°C	1.34%
Vapor temperature from Effect 3	93.6	89.5	°C	4.58%
Vapor temperature from Effect 4	78.3	77.2	°C	1.42%
Vapor temperature from Effect 5	67.1	67.2	°C	0.15%
Vapor temperature from Effect 6	58.3	58.7	°C	0.68%
Vapor temperature from Effect 7	52	52	°C	0.00%
Black liquor dissolved solids from Effect 1	29.17	31.65	%	7.84%
Black liquor dissolved solids from Effect 2	26.59	26.29	%	1.14%
Black liquor dissolved solids from Effect 3	23.08	24.42	%	5.49%
Black liquor dissolved solids from Effect 4	19.59	20.32	%	3.59%
Black liquor dissolved solids from Effect 5	16.66	17.29	%	3.64%
Black liquor dissolved solids from Effect 6	14.67	15.12	%	2.98%
Black liquor dissolved solids from Effect 7	13.24	13.45	%	1.56%
Total live steam mass flow	2.2	1.9	kg/s	15.79%

It should be noted that the steps for ordering the GSOE, partitioning it, and obtaining the initial estimates by solving the simplified model were critical to ensuring that the simulator would converge. In both scenarios, the combining of these steps allowed the simulator to converge with relative ease. This, however, was not the case when partitioning and solving the simplified model were skipped. Solving all the equations simultaneously via the NR method proved to be a particularly poor approach, as poor initial estimates often led to singular jacobians during the NR iterations.

It must also be emphasized that the simulator determines the ordering of the GSOE based on the form taken by each equation, that is, the set of variables present in each equation. In other words, the way the equations are written has a direct impact on how the simulator

performs. The equations described in Table 3.2 are written in a way that yielded the most satisfactory results.

4.3 Expanding the base scenarios using the EOA simulator

Figure 4-3 shows the average number of function evaluations required for S_1 , when the stopping criteria included either reaching the maximum allowed NFE or a solution within 1% of the best solution found by running the DE multiple times with conservative parameter settings that emphasized robustness over speed, that is, large F and very large population size: 2.497×10^5 USD. Due to the simplicity of this scenario, all runs converged at the same point, adding a new evaporator body in series with a heat transfer area of 400 m^2 . This is an interesting observation, because if the system to be optimized is relatively small, DE can find the optimal solution with smaller population sizes, which in turn reduces computation times.

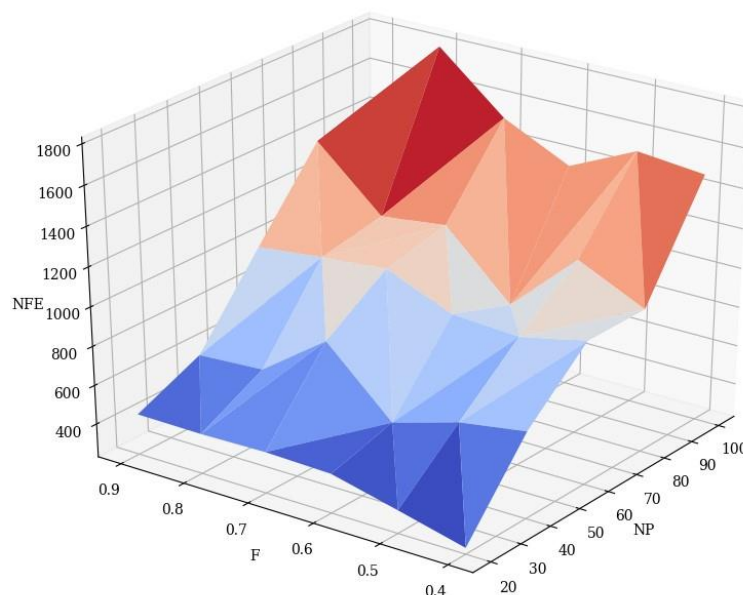


Figure 4-3: Average NFE required to solve S_1 (derived from (Vianna Neto, Saari, *et al.*, 2020)).

The average NFE increased with Np , as expected, since population numbers imply higher NFE counts per generation. The results do not indicate that there is a clear relation between F and NFE. Higher values for F tend to favor convergence reliability over convergence rate (Price, Storn and Lampinen, 2005). Since all S_1 scenarios converged, the effect of F could not be clearly seen.

Figures Figure 4-4 and Figure 4-5 show the best-case and worst-case convergence curves, as measured by the value of f_{obj} until convergence, for solving S_2 . The worst-case curves are the ones which, for a given combination of Np and F , yielded the highest cost.

Conversely, the best-case curves are the ones that yielded the lowest cost for each combination of Np and F . Figures Figure 4-6(a) and Figure 4-6(c) show how the heat transfer areas, A_{par} and A_{ser} , corresponding to evaporators E_{par} and E_{ser} , respectively, evolved for the best-case scenario of S_2 . The evolution of A_{par} and A_{ser} for the worst-case scenarios of S_2 are shown in figures Figure 4-6(b) and Figure 4-6(d). When the methodology was applied to S_1 , A_{par} and A_{ser} converged monotonically at their optimal values in all runs.

Even though convergence was relatively straightforward for S_1 , the same ease does not transfer to more complex scenarios, such as the S_2 scenario. Figures Figure 4-4 and Figure 4-5 show that most, but not all, of the parameter combinations always converged at the identified value, 1.996×10^5 USD. When $F = 0.5$, some runs failed to find this value, as can be seen in the worst-case scenario curves, indicating that this is too greedy a setting and that higher values should be used for F . The optimal solution was adding a new evaporator body in parallel with a heat transfer area of 300 m^2 , in contrast to the optimal solution found for S_1 , where an evaporator body was added in series.

The results above indicate that the proposed methodology can find the optimal arrangement for the new evaporator, whether it be in series or in parallel, thus validating the proposed methodology for the tested systems.

It was interesting to examine the evolution of the optimization variables as the optimization was being carried out. When comparing Figure 4-6(d) with figures Figure 4-4 and Figure 4-5, it is clear that the Np and F pairs whose worst-case scenario curves converged at the optimum also corresponded to A_{ser} converging at 0. The two pairs that converged at a local minimum with a worse f_{obj} also corresponded to a value of A_{ser} on the order of 300 m^2 . Similarly, when comparing Figure 4-6(b) with Figure 4-5 it is clear that all pairs of Np and F converged at a value of A_{par} equal to 300 m^2 . Based on this finding, it is possible to draw two conclusions: a) the optimal arrangement for S_2 consists of adding a new evaporator body in parallel and b) scenarios in which both an evaporator body in series and one in parallel would be added were contemplated at some point during optimization. The latter conclusion is critical, as it proves that the optimizer was indeed capable of testing different configurations as opposed to being trapped in a reduced search space.

The best-case scenario curves displayed in figures Figure 4-6(a) and Figure 4-6(c) show that A_{par} and A_{ser} converged monotonically at the optimal values. In fact, for these runs the optimization could be stopped for NFE values as low as 10^4 . It is interesting to point out that in the best-case scenarios, A_{ser} started off at zero and remained at zero until the end of the optimization.

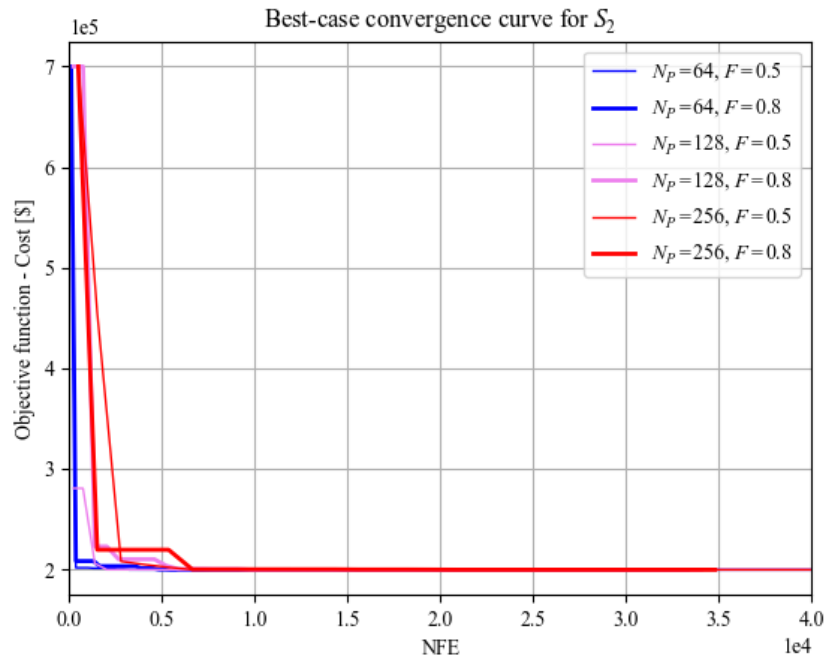


Figure 4-4: Evolution of f_{obj} with NFE for the best-case scenario for S_2 (derived from (Vianna Neto, Cardoso, Vakkilainen, *et al.*, 2020)).

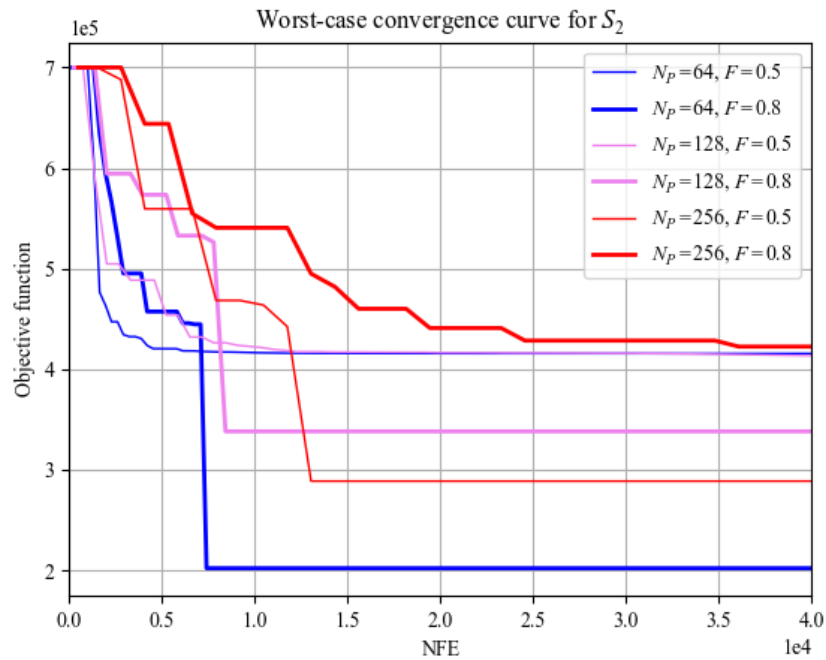


Figure 4-5: Evolution of f_{obj} with NFE for the worst-case scenario for S_2 (derived from (Vianna Neto, Cardoso, Vakkilainen, *et al.*, 2020)).

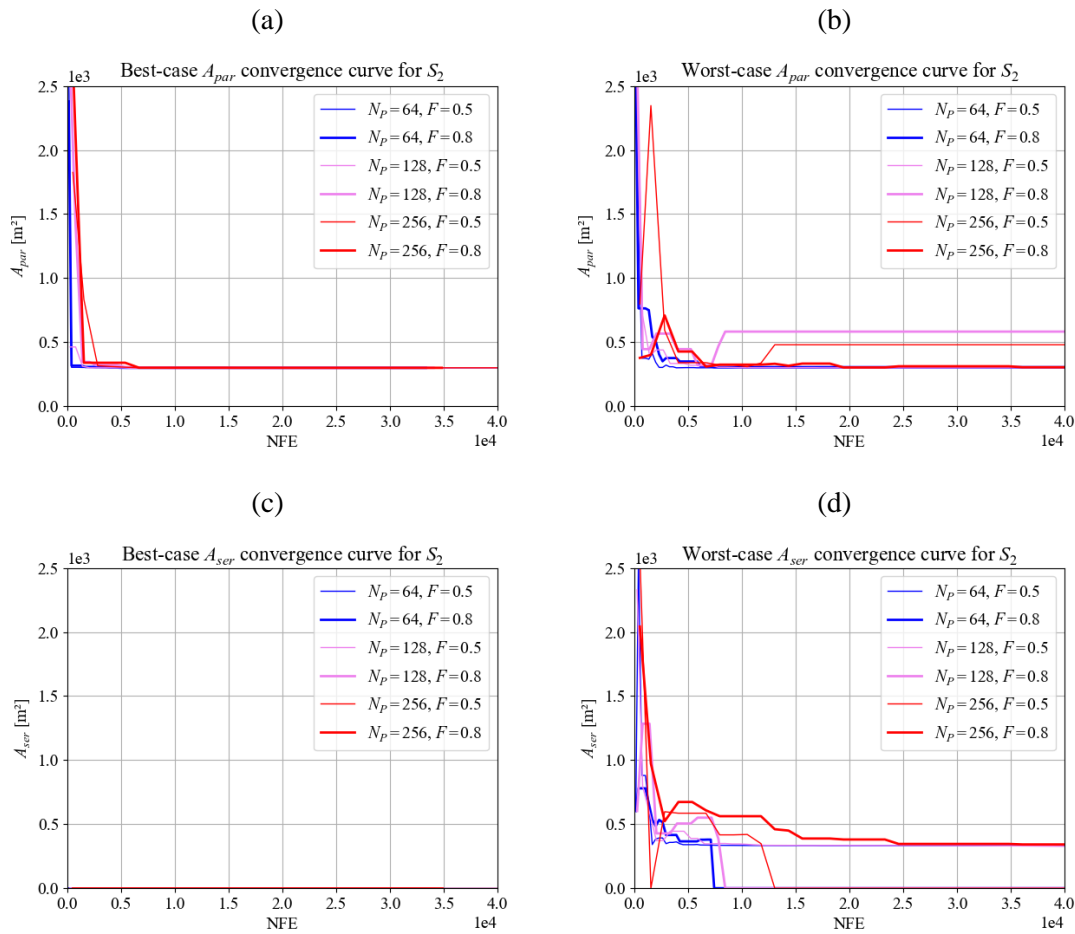


Figure 4-6: Evolution of heat exchange areas A_{par} and A_{ser} for system S_2 versus NFE for the best-case and worst-case scenarios (derived from (Vianna Neto, Cardoso, Vakkilainen, *et al.*, 2020)).

It should be noted that the heat exchange areas of both scenarios converged at their lower bounds. This suggests that adding evaporator bodies whose areas are equal to the lower bounds is more than sufficient to ensure that the systems maintain the same dissolved solids fraction, despite operating at higher black liquor mass flow rates. It is also important to realize that increasing the black liquor flow or changing the lower bounds for the areas may result in different final configurations.

4.4 Improving the convergence characteristics of the EOA simulator

The long plateaus that can be seen in figures Figure 4-6(a)-(d) indicated that the optimizer might have been evaluating scenarios that were hard for the simulator to converge. This observation motivated the search for improvements in the convergence characteristics of the EOA simulator.

Figure 4-7 shows the outlet solids mass fraction of a single evaporator versus its inlet live steam flow and its outlet vapor pressure. It is important to notice that the intended effect of using the modified model was achieved: when there is no live steam inflow, the outlet solids fraction is equal to the inlet solids fraction. This is to be expected, as no evaporation can take place when no live steam is supplied.

This scenario was simple enough that convergence was achieved with the first initial estimate for all calculated values. The graph shows that the new evaporator model can be used to simulate isolated evaporator bodies where no live steam is supplied. This is an important result because it suggests that the new model may be used for simulating larger, more realistic systems, since those would be described by the same mass and energy balances. This was, indeed, shown to be the case, as confirmed by the results obtained by solving the larger systems.

The three-effect system was also successfully solved. However, since this system is more complex when compared with the single evaporator scenario, its corresponding GSOE was larger, thus making the problem more challenging to solve, as would be expected. Unlike the single evaporator scenario, some initial estimates did not lead to convergence. The summary statistics for the number of random initial estimates that were necessary for convergence are listed in Table 4.3. The sample space was taken as the set of all simulated scenarios. It should be noted that, even though it may be necessary to repeatedly try initial estimates, convergence could be achieved for all scenarios.

Table 4.3: Summary statistics for the number of trials required for the three-effect MEE system to converge (derived from (Vianna Neto, Márcio R Cardoso, Vakkilainen and Oliveira, 2020)).

Variable	Value
Average	436.4
Standard deviance	1 238.4
Maximum	11 413
Minimum	1

A striking feature shown in Table 4.3 is the high variability in the necessary initial estimates for convergence, which was on the order of three standard deviances. The simulation could converge on the first try or take as long as 11,000 estimates. On average, however, 400 estimates were sufficient. This difficulty can be traced back to two factors: a) the fact that the initial estimates for all variables were chosen at random and b) that equation 3.30 introduces a discontinuity in the GSOE, which may cause the Jacobian matrix to become singular during the solution process. This discontinuity is due to the *if* statement, which radically changes the variables that are involved in that equation. For this reason, at points close to the boiling/non-boiling transition, there is a chance that the Jacobian would be non-invertible, causing it to fail to correctly guide the NR method or resulting in the fact that the numerically calculated derivatives would not be accurate at all.

Outlet liquor dry solids fraction for a single evaporator body

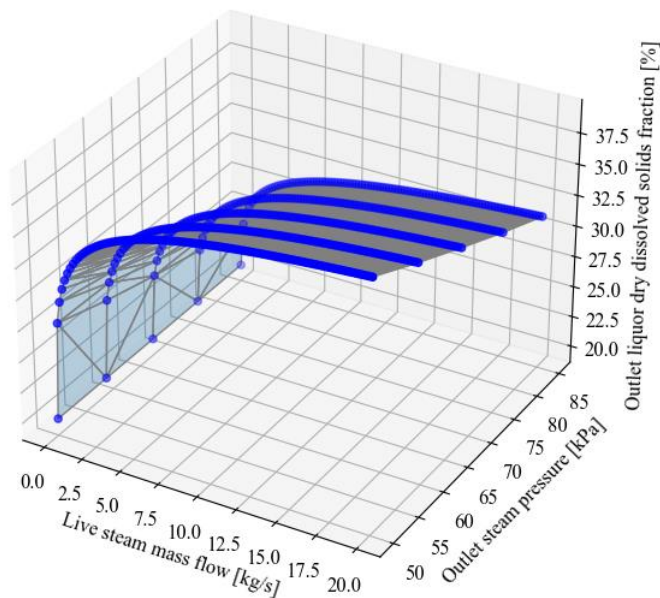


Figure 4-7: Outlet solids mass fraction versus live steam mass flow and outlet vapor pressure for a single evaporator (derived from (Vianna Neto, Márcio R Cardoso, Vakkilainen and Oliveira, 2020)).

It may be possible to minimize these problems by systematically generating better initial estimates using, for instance, a simplified model or by attempting to make the numerical solution method more robust. For that purpose, using analytically calculated derivatives may be helpful.

Figure 4-8 shows the calculated inlet and outlet black liquor solids fractions corresponding to each effect as a function of the live steam mass flow for a fixed heat transfer area of $A = 1,000 \text{ m}^2$. All values displayed in the graph correspond to runs that converged. Notice that the black liquor dry dissolved solids fraction curves are smooth. Had there been numerical instabilities, or had the GSOE been ill-posed, the curves might have displayed a jagged appearance.

As would be expected, solids fractions increase with the effect number and with live steam flow. This behavior replicates what is shown in Figure 4-7. More importantly, the model was capable of simulating scenarios where the live steam flow was low, yielding sensible results.

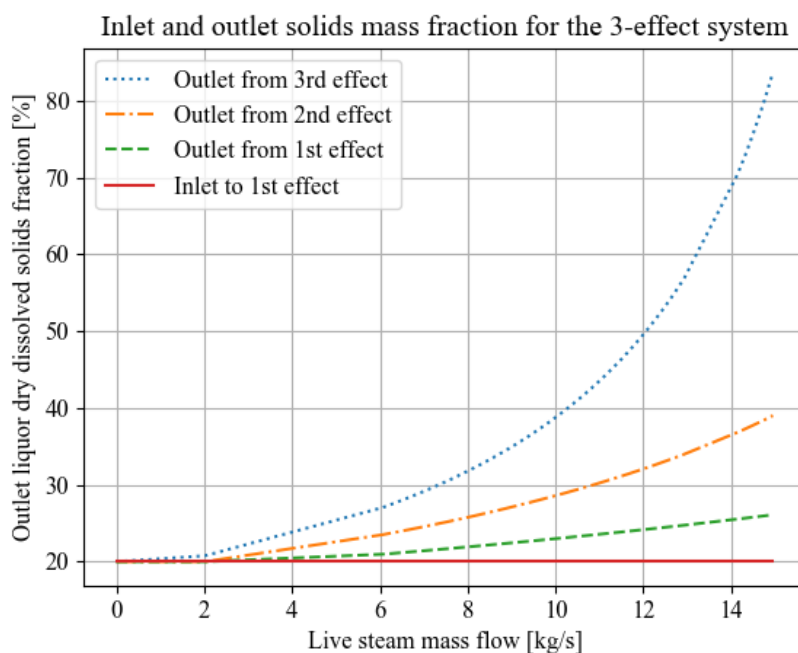


Figure 4-8: Inlet and outlet solids mass fraction versus live steam mass flow for the three-effect system ($A = 1\,000\text{ m}^2$) (derived from (Vianna Neto, Cardoso, Sermiyagina, *et al.*, 2020)).

The seven-effect scenario was, as expected, more difficult to converge, taking no less than 400 initial estimates to converge. The reasons for this behavior are the same: initial estimates were randomly sampled for the occurrence of singular Jacobians close to the boiling/non-boiling transition, which becomes more likely as the number of variables increases. Some key calculated results for this scenario are shown in Table 4.4.

Table 4.4: Summarized results for the seven-effect MEE system (derived from (Vianna Neto, Cardoso, Sermiyagina, *et al.*, 2020)).

Variable	Value	Units
Outlet vapor temperature from Effect 7	68.0	°C
Black liquor outlet mass flow from Effect 1	6.6	kg/s
Black liquor outlet temperature from Effect 1	104.8	°C
Outlet dissolved solids from Effect 1	49.4	%
Outlet dissolved solids from Effect 2	38.7	%
Outlet dissolved solids from Effect 3	32.7	%
Outlet dissolved solids from Effect 4	28.6	%
Outlet dissolved solids from Effect 5	25.6	%
Outlet dissolved solids from Effect 6	23.4	%
Outlet dissolved solids from Effect 7	21.6	%

4.5 Convergence characteristics of the SMA simulator

The results obtained with the SMA simulator were the most reliable of all. The simulator converged for every tested scenario using initial estimates derived from typical values and the convergence occurred in under 100 iterations.

Figure 4-9 shows the number of iterations required for each system to converge for different live steam mass flows. The number of iterations ranged from ten for the three-effect system to almost 100 for the seven-effect system. As mentioned before, the SMA simulator behaved quite reliably, converging for all scenarios. It is worth mentioning that this reliability took place despite not resorting to simplified models, as was done originally in the EOA simulator.

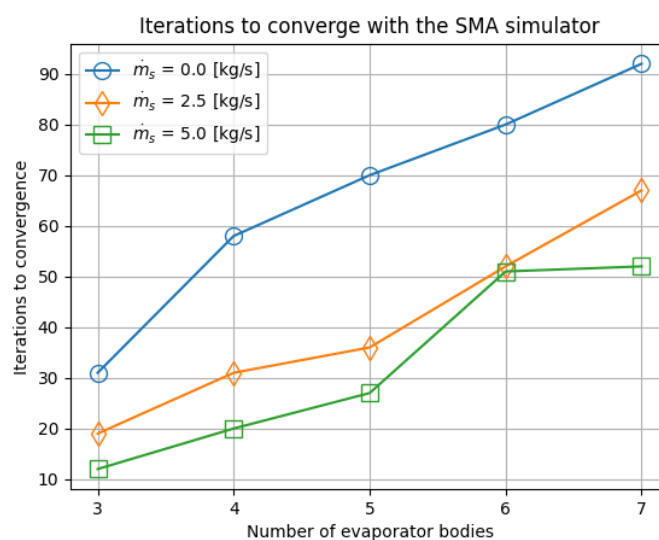


Figure 4-9: Number of iterations required for each system to converge (adapted from (Vianna Neto, Cardoso, Sermyagina, *et al.*, 2020)).

The number of iterations increases as the systems grow larger. This is to be expected because larger systems require more recycles to be torn and, therefore, more convergence variables to converge. An interesting feature that can be seen in Figure 4-9 is that the number of iterations grows as the live steam mass flow approaches zero. When the steam mass flow values are low, the evaporator modules alternate between letting off steam and not evaporating at all as the iterations proceed. This is the same difficulty encountered when dealing with the EOA simulator. This switching behavior slows convergence and causes the number of iterations to increase. However, in the SMA runs convergence was

slowed down, but not prevented. This indicates that the SMA simulator is far more robust when dealing with the threshold where boiling begins to take place.

Wegstein's method gave very good and reliable results, in contrast with the simpler fixed-point iteration scheme, which rarely converged. Wegstein's method is less expensive from a computational standpoint when compared to NR, and, at the same time, more robust than fixed-point iterations, since it does not require a full jacobian matrix to be recalculated at each step, but still attempts to estimate derivatives using information from earlier iterations. Since it is faster to evaluate than NR, but still converges satisfactorily, it should be the preferred method.

The number of iterations required to solve the tested systems can easily be handled by common desktop computers, since the running times are relatively low. This can be seen in Figure 4-10, which shows the mean computational time in milliseconds required for each system to converge over 100 runs. The vertical bars shown in the figure are standard deviations.

Note that running times range from 5ms to 50ms, thus allowing it to be used within optimization algorithms. Standard deviations are relatively small, on the order of 5ms, being most noticeable in the five-effect scenarios. As would be expected, running times increase as the systems grow larger. This is a direct consequence of the larger iteration numbers needed for convergence.

Computational time to converge with the SMA simulator

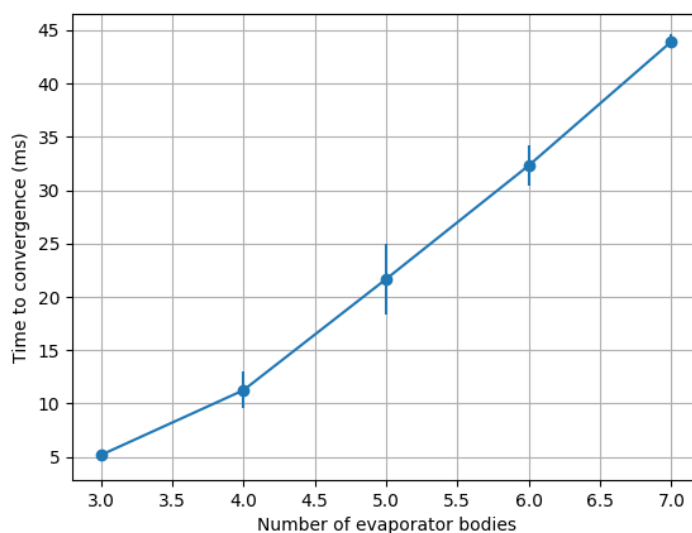


Figure 4-10: Mean computational time in milliseconds required for each system to converge over 100 runs. The vertical bars denote standard deviations (adapted from (Vianna Neto, Cardoso, Sermyagina, *et al.*, 2020)).

4.6 Discussion

4.6.1 Theoretical implications

The answers to the key questions posed at the beginning of the thesis can be stated as follows:

Question a) What mathematical difficulties arise when modeling an evaporator system?

Paper I argued that to facilitate convergence, it is desirable to make sure that the equations take a suitable form and that they be ordered and partitioned. If no good initial estimates can be given, it is also desirable to solve a simplified model to generate reasonable estimates. The importance of these measures cannot be overstated since the high nonlinearity of the evaporator model can easily cause divergence.

Optimization using differential evolution requires that the evaporator model often be solved more than several thousand times. To speed up calculations, one should not solve all parameters during all calculation rounds. (Vianna Neto, Saari, *et al.*, 2020) have suggested that the heat transfer coefficient should be given by the user as opposed to being calculated by the simulator. In the future, this constraint may be relaxed by introducing heat transfer correlations that are periodically updated.

Question b) What numerical methods are best suited to solving the model?

The NR method proved effective when calculating evaporator systems with the equation-oriented approach, as can be seen in publications by (Vianna Neto, Cardoso, Vakkilainen, *et al.*, 2020) and (Vianna Neto, Márcio R Cardoso, Vakkilainen and Oliveira, 2020). If evaporator optimization is to be done in the manner discussed by (Vianna Neto, Saari, *et al.*, 2020), however, trust-region methods tend to be more robust. In a sequential-modular architecture, Wegstein's method gave very good and reliable results, in contrast with the simpler fixed-point iteration scheme, which rarely converged. Since it is faster to evaluate than NR, but still converges satisfactorily, it should be the preferred method.

Question c) Is differential evolution well suited to performing this type of optimization? If so, are there any optimal ranges for its parameters?

Differential evolution was shown to be suitable for this type of problem, even though it might require parameter tuning. No clear optimal parameter ranges were verified. However, it should be noted that the proposed methodology may lead to local optima, and higher F values should be preferred.

Question d) How well does the proposed methodology scale as the problems grow more complex?

The proposed optimization methodology was tested with a simple scenario and a more comprehensive and realistic scenario, and it successfully optimized both. As was expected, difficulty increased with scenario complexity, but this did not hinder its applicability. (Vianna Neto, Saari, *et al.*, 2020) have proposed that in future studies, more unit processes can be modeled, such as condensate preheaters and recovery boilers, which would allow for more realistic scenarios to be simulated. More complex systems should also be tested to verify whether the current solution strategy remains robust.

4.6.2 Practical implications

In this dissertation, a practical sequential-modular method for rapidly solving evaporator trains was developed. This method, when used with Wegstein's method, was shown to be very effective for calculating evaporator systems. The simulator architecture is also versatile enough to be expanded and accommodate other unit processes.

The development of a simulation engine is a complex procedure, but if done correctly, it should be general enough to allow the user to be able to add new models with relative ease. If the proposed methodology is to be applied in practice, users should be able to implement their models without having to reimplement the engine from scratch. Keeping this in mind, the sequential-modular engine will be made publicly available in open-source format, with the hope that it will make the proposed methodology more easily usable.

It should be noted that the simulation engine is general enough that it can be used for simulating processes other than evaporation systems. An obvious candidate are steam power cycles, as steam table calculation have already been implemented. Future studies should be done with the simulation engine to assess how robust it is for solving other processes.

Differential evolution proved suitable for this type of problem, even though it might require parameter tuning. No clear optimal parameter ranges were verified. However, it should be noted that the proposed methodology may lead to local optima, and higher F values should be preferred.

Both the EOA and SMA simulators can be improved in many ways. In their current implementation, it is assumed that the heat transfer coefficient is given by the user, as opposed to being calculated by the simulator. In the future, this issue may be addressed by introducing heat transfer correlations. In future work, more unit processes can be modeled, such as condensate preheaters and recovery boilers, which would allow for more realistic scenarios to be simulated.

More specifically, with respect to the sequential-modular simulator, more complex systems should also be tested to verify whether the current solution strategy remains robust and scales well. Finally, the same optimization methodology as applied to the equation-oriented simulator should be tested using the sequential-modular simulator.

5 Conclusions

The research hypothesis was confirmed in this study. Indeed, a methodology for simultaneously optimizing evaporator systems based on their topological arrangement and other internal design variables was presented, and a realistic evaporator system expansion scenario was successfully optimized.

The methodology made use of an equation-oriented simulator capable of simulating a wide array of evaporator arrangements. To facilitate convergence, it is important to make sure that the equations take a suitable form, as different formulations lead to different convergence behaviors, and that they are ordered and partitioned. If no good initial estimates can be given, it is also desirable to solve a simplified model to generate reasonable estimates.

The methodology, however adequate, caused plateaus in the objective function evolution graphs. This was attributed to mathematical convergence issues in corner cases where the evaporators transitioned from being at a non-boiling state to a boiling state. This issue was partially addressed, but not completely solved, by changing the original evaporator model formulation. The changes were effective for small systems, but ineffective for realistically sized systems.

Changing the simulator design to a sequential-modular design, however, drastically increased convergence rates, and the results indicate that this should be the preferred simulation architecture for the optimization of topological evaporator systems. The results also indicate that this architecture solves the scaling issues that were verified with the equation-oriented architecture, as all simulations were successfully completed in fractions of a second.

Differential evolution was shown to be suitable for this type of problem, even though it might require parameter tuning.

Both simulators can be improved in many ways, such as by introducing heat transfer correlations. In the future, more unit processes can be modeled, such as condensate preheaters and recovery boilers, which would allow for more realistic scenarios to be simulated.

References

- Adams, T. N. *et al.* (1997) *Kraft recovery boilers*. Atlanta, United States: TAPPI Press.
- Adams, T. N. (2001) ‘Sodium salt scaling control in black liquor evaporators and concentrators’, *Tappi journal*, p. 18.
- Adams, T. N. and Frederick, W. J. (1988) *Kraft recovery boiler physical and chemical processes*. New York, United States.
- Adib, T. A., Heyd, B. and Vasseur, J. (2009) ‘Experimental results and modeling of boiling heat transfer coefficients in falling film evaporator usable for evaporator design’, *Chemical Engineering and Processing: Process Intensification*, 48(4), pp. 961–968.
- Afanasyeva, S. *et al.* (2013) ‘Optimization of wind farm design taking into account uncertainty in input parameters’, in *Proceedings of the European Wind Energy Conference and Exhibition*, pp. 1–10.
- Alhusseini, A. A., Tuzla, K. and Chen, J. C. (1998) ‘Falling film evaporation of single component liquids’, *International journal of heat and mass transfer*, 41(12), pp. 1623–1632.
- Almeida, G. M. de *et al.* (2000) ‘Estudo da influência das variáveis operacionais da caldeira de recuperação sobre a geração de vapor utilizando redes neurais artificiais’, in *ABTCP, 35th Annual Pulp and Paper Congress and Exposition*.
- Andersson, M. (2015) *Modelling of Black Liquor Evaporator Cleaning*. Chalmers University.
- Andreuccetti, M. T., Leite, B. S. and D’Angelo, J. V. H. (2011) ‘Eucalyptus black liquor—Density, viscosity, solids and sodium sulfate contents revisited’, *O Papel*, 72(12), pp. 52–57.
- Bajpai, P. (2016) *Pulp and paper industry: energy conservation*. Elsevier.
- Bhargava, R. *et al.* (2008) ‘Simulation of flat falling film evaporator system for concentration of black liquor’, *Computers and Chemical Engineering*, 32(12), pp. 3213–3223.
- Biegler, L. T., Grossmann, I. E. and Westerberg, A. W. (1997) ‘Systematic methods for chemical process design’.
- Billet, R. and Fullarton, J. W. (1989) *Evaporation technology: principles, applications, economics*. 1st edn. New York: VCH Publishers.

- Boyd, S. and Vanderberghe, L. (2004) *Convex Optimization*. 1st edn. Cambridge: Cambridge University Press.
- Broberg, A. (2012) 'Experimental investigation and modelling of sodium scale dissolution rates in black liquor evaporators'.
- Cardoso, M. *et al.* (2009) 'Chemical process simulation for minimizing energy consumption in pulp mills', *Applied Energy*, 86(1), pp. 45–51.
- Cardoso, M., de Oliveira, É. D. and Passos, M. L. (2009) 'Chemical composition and physical properties of black liquors and their effects on liquor recovery operation in Brazilian pulp mills', *Fuel*, 88(4), pp. 756–763.
- Chantasiriwan, S. (2015) 'Optimum surface area distribution in co-current multiple-effect evaporator', *Journal of Food Engineering*, 161, pp. 48–54.
- Chen, F. C. and Gao, Z. (2004) 'An analysis of black liquor falling film evaporation', *International Journal of Heat and Mass Transfer*, 47(8–9), pp. 1657–1671.
- Cooper, J. R. *et al.* (2007) *Revised Release on the IAPWS Industrial Formulation 1997 for the Thermodynamic Properties of Water and Steam*. Lucerne.
- Costa, A. O. S., Biscaia Jr, E. C. and Lima, E. L. (2004) 'Mathematical description of the kraft recovery boiler furnace', *Computers & chemical engineering*, 28(5), pp. 633–641.
- da Costa, A. O. S. *et al.* (2016) 'Empirical analysis of the boiling point elevation of eucalyptus kraft black liquor', *O Papel*, 77(10), pp. 88–92.
- Costa, G. A. A. *et al.* (2007a) 'Overall Heat Transfer Coefficients in a Kraft Black Liquor Industrial Evaporation Unit: Part I-Simulation of Multiple Effect Evaporation System', *Appita: Technology, Innovation, Manufacturing, Environment*, 60(4), p. 321.
- Costa, G. A. A. *et al.* (2007b) 'Overall Heat Transfer Coefficients in a Kraft Black Liquor Industrial Evaporation Unit: Part II-Predictive Correlations', *Appita: Technology, Innovation, Manufacturing, Environment*, 60(4), p. 327.
- Ding, X. *et al.* (2009) 'Evaporator modeling - A hybrid approach', *Applied Energy*, 86(1), pp. 81–88.
- Feller, W. (1957) *An introduction to probability theory and its applications*. 3rd edn. Hoboken, New Jersey, United States: John Wiley & Sons.
- Ferreira, D. J. O., Cardoso, M. and Park, S. W. (2010) 'Gas flow analysis in a Kraft recovery boiler', *Fuel Processing Technology*, 91(7), pp. 789–798.
- Floudas, C. A. (2013) *Deterministic global optimization: theory, methods and*

applications. Dordrecht: Springer Science & Business Media.

Frederick, W. J. *et al.* (2004) 'Crystallization and control of sodium salt scales in black liquor concentrators', *Tappi journal* (2002), 3(6), pp. 7–13.

Frishman, Y. and Tal, A. (2009) *Graph Drawing Algorithms in Information Visualization*. Computer Science Department, Technion.

Fritzson, P. (2010) *Principles of object-oriented modeling and simulation with Modelica 2.1*. John Wiley & Sons.

Gämperle, R., Müller, S. D. and Koumoutsakos, P. (2002) 'A parameter study for differential evolution', *Advances in intelligent systems, fuzzy systems, evolutionary computation*, 10(10), pp. 293–298.

Ghosh, A. *et al.* (2017) 'A switched parameter differential evolution with optional blending crossover for scalable numerical optimization', *Applied Soft Computing*, 57, pp. 329–352.

Gourdon, M. and Mura, E. (2017) 'Performance evaluation of falling film evaporators in the dairy industry', *Food and Bioproducts Processing*, 101, pp. 22–31.

Järvinen, M. P. *et al.* (2015) 'Vapor pressure and boiling point elevation of black liquor', *Nordic Pulp & Paper Research Journal*, 30(3), pp. 411–416.

Ji, X. *et al.* (2012) 'Simulation and energy optimization of a pulp and paper mill - Evaporation plant and digester', *Applied Energy*, 97, pp. 30–37.

Johansson, M., Vamling, L. and Olausson, L. (2009) 'Heat transfer in evaporating black liquor falling film', *International Journal of Heat and Mass Transfer*, 52(11–12), pp. 2759–2768.

Jyoti, G. and Khanam, S. (2014) 'Simulation of heat integrated multiple effect evaporator system', *International Journal of Thermal Sciences*, 76, pp. 110–117.

Karlsson, E. *et al.* (2013) 'Heat transfer for falling film evaporation of black liquor up to very high Prandtl numbers', *International Journal of Heat and Mass Transfer*, 65, pp. 907–918.

Karlsson, E. (2017) *The Formation and Dissolution of Sodium Salt Scales in Black Liquor Evaporators*. Chalmers University of Technology.

Karlsson, E., Gourdon, M. and Vamling, L. (2016) 'Separation and recirculation of bulk crystals to potentially mitigate sodium salt scaling in black liquor evaporators', 31(4).

Kaya, D. and Ibrahim Sarac, H. (2007) 'Mathematical modeling of multiple-effect evaporators and energy economy', *Energy*, 32(8), pp. 1536–1542.

Kermani, M. *et al.* (2016) 'A novel MILP approach for simultaneous optimization of water and energy: Application to a Canadian softwood Kraft pulping mill', *Computers & Chemical Engineering*.

Khademi, M. H., Rahimpour, M. R. and Jahanmiri, A. (2009) 'Simulation and optimization of a six-effect evaporator in a desalination process', *Chemical Engineering and Processing: Process Intensification*, 48(1), pp. 339–347.

Khanam, S. and Mohanty, B. (2010) 'Energy reduction schemes for multiple effect evaporator systems', *Applied Energy*, 87(4), pp. 1102–1111.

Luenberger, D. G., Ye, Y. and others (2010) *Linear and nonlinear programming*. 3rd edn. New York, United States: Springer.

Mah, R. S. H. (2013) *Chemical process structures and information flows*. Stoneham, United States: Butterworth-Heinemann.

'MATLAB Optimization Toolbox' (2018). Natick, MA, USA: The MathWorks.

Mesfun, S. and Toffolo, A. (2015) 'Integrating the processes of a Kraft pulp and paper mill and its supply chain', *Energy Conversion and Management*, 103, pp. 300–310.

Olsson, M. R. (2009) *Simulations of Evaporation Plants in Kraft Pulp Mills Including Lignin Extraction and Use of Excess Heat*.

Price, K. V., Storn, R. M. and Lampinen, J. A. (2005) *Differential Evolution: A Practical Approach to Global Optimization*. Berlin/Heidelberg: Springer-Verlag (Natural Computing Series).

Ramamurthy, P., Van Heiningen, A. R. P. and Kubes, G. J. (1993) 'Viscosity and thermal conductivity of black liquor', *Tappi journal*, 76(11), pp. 175–179.

Ronkkonen, J., Kukkonen, S. and Price, K. V (2005) 'Real-parameter optimization with differential evolution', in *2005 IEEE congress on evolutionary computation*, pp. 506–513.

Saari, J. *et al.* (2014) 'Heat Transfer Model and Optimization of a Shell-And-Tube District Heat Condenser', in *Proceedings of the 27th International Conference on Efficiency, Cost, Optimization, Simulation and Environmental Impact of Energy Systems (ECOS)*, pp. 1920–1933.

Saari, J. *et al.* (2019) 'Shell-and-tube heat exchanger optimization-impact of problem formulation and cost function', in *14th International Conference on Heat Transfer, Fluid*

Mechanics and Thermodynamics HEFAT. Wicklow, Ireland: HEFAT, p. 7.

Saturnino, D. M. (2012) *Modeling of Kraft Mill Chemical Balance*. University of Toronto. Available at: <https://tspace.library.utoronto.ca/handle/1807/32881>.

Sedgewick, R. and Wayne, K. (2011) *Algorithms*. 4th edn. Upper Saddle River, New Jersey, United States: Addison-Wesley Professional.

Shi, B. and Rousseau, R. W. (2003) 'Structure of burkeite and a new crystalline species obtained from solutions of sodium carbonate and sodium sulfate', *The Journal of Physical Chemistry B*, 107(29), pp. 6932–6937.

Smith, R. (2016) *Chemical process: design and integration*. 2nd edn. Chichester, United Kingdom: John Wiley & Sons.

Soemardji, A. P. *et al.* (2004) 'Prediction of crystal species transition in aqueous solutions of Na₂CO₃ and Na₂SO₄ and kraft black liquor', *Tappi journal* (2002), 3(11), pp. 27–32.

Storn, R. (1996) 'On the usage of differential evolution for function optimization', *Biennial Conference of the North American Fuzzy Information Processing Society, 1996 (NAFIPS)*, pp. 519–523.

Tikka, P. (2008) *Chemical pulping part 2: recovery of chemicals and energy*. 2nd edn. Edited by P. Tikka. Helsinki: Paper Engineers' Association/Paperi ja Puu Oy.

Vakkilainen, E. K. (2007) *Kraft recovery boilers - Principles and practice*. Edited by Suomen Soodakattilayhdistys r.y. Helsinki.

Vakkilainen, E. K. (2016) *Steam generation from biomass: construction and design of large boilers*. Butterworth-Heinemann.

Verma, O. P., Manik, G. and Sethi, S. K. (2019) 'A comprehensive review of renewable energy source on energy optimization of black liquor in MSE using steady and dynamic state modeling, simulation and control', *Renewable and Sustainable Energy Reviews*, 100, pp. 90–109.

Vianna Neto, Márcio R Cardoso, M., Vakkilainen, E. K. and Oliveira, É. D. (2020) 'Improving an equation-oriented steady-state evaporation plant simulator with a more robust evaporator model', in *International Chemical Recovery Conference*.

Vianna Neto, M. R., Saari, J., *et al.* (2020) 'A superstructure-based methodology for simultaneously sizing and arranging additional evaporator bodies in multiple-effect evaporator plants', *Journal of Science & Technology for Forest Products and Processes*, 7(6), pp. 36–47.

Vianna Neto, M. R., Cardoso, M., Sermyagina, E., *et al.* (2020) 'Designing a sequential-

modular steady-state simulator for Kraft recovery cycle evaporative systems', in *The 53rd Pulp and Paper International Congress and Exhibition*.

Vianna Neto, M. R., Cardoso, M., Vakkilainen, E. K., *et al.* (2020) 'Development of an equation-oriented steady-state evaporation plant simulator', *O Papel*, 81(07), pp. 83–89.

Westerberg, A. W. *et al.* (1979) *Process flowsheeting*. 1st edn. New York: Cambridge University Press.

Yang, X.-S. (2010) *Nature-inspired metaheuristic algorithms*. Luniver press.

Zaman, A., Wight, M. O. and Fricke, A. L. (1994) 'Density and thermal expansion of black liquors', *Tappi Journal*, 77(8), pp. 175–181.



Márcio Ribeiro Vianna Neto

Synthesis and optimization of Kraft process evaporator plants

Síntese e otimização de plantas de evaporação no processo Kraft

Dissertation for the degree of Doctor of Science (Technology) to be presented with due permission for public examination and criticism at Lappeenranta-Lahti University of Technology LUT, Lappeenranta, Finland on the 9th of March, 2021, at 4 PM, Finnish time.

The dissertation was written under a joint supervision (cotutelle) agreement between Lappeenranta-Lahti University of Technology LUT, Finland and the Federal University of Minas Gerais, Brazil and jointly supervised by supervisors from both universities.

Supervisors Professor Esa Kari Vakkilainen
LUT School of Energy Systems
Lappeenranta-Lahti University of Technology LUT
Finland

Professor Éder Domingos Oliveira
Chemical Engineering Department
Universidade Federal de Minas Gerais UFMG
Brazil

Reviewers Professor Nikolai DeMartini
Department of Chemical Engineering & Applied Chemistry
University of Toronto
Canada

PhD Song Won Park
Department of Chemical Engineering
University of São Paulo
Brazil

Opponents Professor Nikolai DeMartini
Department of Chemical Engineering & Applied Chemistry
University of Toronto
Canada

Professor Daniel Saturnino
Department of Mining and Environmental Engineering
Federal University of South and Southeast Pará
Brazil

Publication I

Vianna Neto, M. R., Saari, J., Vakkilainen, E., Cardoso, M., and Oliveira, E.
**A superstructure-based methodology for simultaneously sizing and arranging
additional evaporator bodies in multiple-effect evaporator plants**

Reprinted with permission from

The Journal of Science and Technology for Forest Products and Processes

Vol. 7, pp. 36-47, 2020

© 2020, PAPTAC

Publication II

Vianna Neto, Cardoso, M., Vakkilainen, E., and Oliveira, E.

Development of an equation-oriented steady-state evaporation plant simulator

Reprinted with permission from

O Papel

Vol. 81, pp. 83-89, 2020

© 2020, ABTCP